Assessment of the accuracy of microphone array methods for aeroacoustic measurements

Merino-Martínez, Roberto; Luesutthiviboon, Salil; Zamponi, Riccardo; Rubio Carpio, Alejandro; Ragni, Daniele; Sijtsma, Pieter; Snellen, Mirjam; Schram, Christophe

DOI
10.1016/j.jsv.2020.115176

Publication date
2020

Document Version
Final published version

Published in
Journal of Sound and Vibration

Citation (APA)
Merino-Martínez, R., Luesutthiviboon, S., Zamponi, R., Rubio Carpio, A., Ragni, D., Sijtsma, P., Snellen, M., & Schram, C. (2020). Assessment of the accuracy of microphone array methods for aeroacoustic measurements. *Journal of Sound and Vibration*, *470*, Article 115176. https://doi.org/10.1016/j.jsv.2020.115176

Journal of Sound and Vibration 470 (2020) 115176

Contents lists available at ScienceDirect

Journal of Sound and Vibration

journal homepage: www.elsevier.com/locate/jsvi

Assessment of the accuracy of microphone array methods for aeroacoustic measurements

Roberto Merino-Martínez [a,*], Salil Luesutthiviboon [a], Riccardo Zamponi [b], Alejandro Rubio Carpio [a], Daniele Ragni [a], Pieter Sijtsma [a,c], Mirjam Snellen [a], Christophe Schram [b]

[a] Faculty of Aerospace Engineering, Delft University of Technology, Kluyverweg 1, 2629 HS, Delft, the Netherlands
[b] Environmental and Applied Fluid Dynamics Department, von Karman Institute for Fluid Dynamics, 1640, Sint-Genesius-Rode, Belgium
[c] Pieter Sijtsma Advanced AeroAcoustics (PSA3), 8091 AV, Wezep, the Netherlands

ARTICLE INFO

Article history:
Received 14 May 2019
Revised 4 November 2019
Accepted 4 January 2020
Available online 7 January 2020
Handling Editor: P. Joseph

MSC[2010]:
00-01
99-00

Keywords:
Microphone arrays
Aeroacoustics
Acoustic imaging

ABSTRACT

In this paper, the performance of four acoustic imaging methods: conventional frequency domain beamforming (CFDBF), functional beamforming (FUNBF), enhanced high resolution CLEAN–SC (EHR–CLEAN–SC) and generalized inverse beamforming (GIBF), is investigated in terms of accuracy and variability. Three experimental test cases are considered: 1) a single speaker emitting synthetic broadband noise, 2) two speakers emitting incoherent synthetic broadband noise, and 3) trailing–edge noise generated by a tripped NACA 0018 airfoil. All the measurements were performed in the anechoic wind tunnel of Delft University of Technology. Overall, GIBF and EHR–CLEAN–SC offer the most accurate results when point sources (speakers) are present. They even achieve super–resolution by separating sound sources beyond the Rayleigh resolution limit. Repeating the measurements indicates a standard deviation in the results of less than 1 dB. When analyzing distributed sound sources, such as trailing–edge noise, CFDBF and FUNBF provide the best performance. This indicates that the acoustic imaging method needs to be selected based on the expected sound source configuration.

1. Introduction

Phased microphone arrays have become one of the main measurement devices for studying aeroacoustic noise sources [1], such as aircraft [2–12], wind turbine blades [13–19], and rotating machinery [20–22]. In combination with acoustic imaging algorithms [1,23], phased microphone arrays provide estimates of the location and strength of sound sources [24,25].

A vast list of acoustic imaging methods [1,23] exists in literature, typically tailored for specific applications or noise sources. Previous research [26] featuring simulated data showed that different imaging methods applied to the same microphone array recording data provided considerably different results. Even when different researchers applied the same method to a given data set, remarkable differences were found [26], indicating an undesirable lack of robustness. One cause for the differences found might be that several formulations are available for parameters, such as the steering vector [27], each of them with advantages and limitations for different applications. Sarradj et al. [28] concluded, after an exhaustive study with synthetic data, that the best method also depends on the frequency of interest. Hence, there is a clear interest in assessing the performance of acoustic

* Corresponding author.
E-mail address: r.merinomartinez@tudelft.nl (R. Merino-Martínez).

https://doi.org/10.1016/j.jsv.2020.115176
0022-460X/

imaging methods in different practical applications, in terms of quality of the source maps, repeatability of the results and accuracy of the source power estimations.

In this paper, this assessment is limited to four acoustic imaging methods:

1. **Conventional frequency domain beamforming (CFDBF)** [24,29,30] is based on the phase differences between the signals recorded by each microphone of the array [4]. It considers a scan grid of potential sound sources and performs an exhaustive search: for each grid point, the agreement between the expected solution for a sound source at that location and the actual signals recorded by the array is evaluated. This method is widely–used since it is robust, intuitive and computationally inexpensive. However, CFDBF is restricted by the Rayleigh resolution limit [31], i.e., the minimum distance at which two sound sources can be distinguished, and is subject to high sidelobe levels, especially at high frequencies. Integration methods have been proposed [32,33], such as the Source Power Integration (SPI) technique [25,34], for defining the results when analyzing spatially distributed sound sources within a region of integration (ROI).
2. **Functional beamforming (FUNBF)** [35,36] provides a higher dynamic range (or lower sidelobe level) and array spatial resolution than CFDBF. This technique raises the CFDBF source map to the power of an exponent parameter ν and the cross–spectral matrix (CSM) to the inverse of this power $1/\nu$. For this paper, the value of ν was selected to be 8 after performing a sensitivity analysis [4,5]. Comparative studies [4,5,23] with other acoustic imaging methods showed that functional beamforming provides better results when applied to aircraft flyover measurements. The functional beamforming source maps can be integrated in a similar way as those from CFDBF [8,9].
3. **Enhanced high resolution CLEAN–SC (EHR–CLEAN–SC)** [37–41] is the high–resolution version of the deconvolution technique CLEAN–SC [42], which uses the fact that the sidelobes are spatially coherent with the main lobe to iteratively *clean* the source map obtained with CFDBF. HR–CLEAN–SC is a super–resolution method, i.e., it increases the spatial resolution of the standard CLEAN–SC beyond the Rayleigh resolution limit. HR–CLEAN–SC achieves this by relocating the source location marker from the actual source location to a location on the main lobe where the combined influence of the other sound sources is the lowest [38,39]. The number of expected sound sources has to be selected by the user. When this is not known, this parameter can be approximated based on the number of the dominant eigenvalues of the CSM. This method has been successfully applied to laboratory tests with speakers [40,41] and open–jet wind–tunnel measurements of a full–scale landing gear [9]. Recent studies [40,41] have also introduced the *Enhanced* version of HR–CLEAN–SC (EHR–CLEAN–SC), which makes use of the low–sidelobe microphone array design to give more freedom in relocating the source marker to widen the frequency range below the Rayleigh resolution limit for which closely–spaced sound sources can be resolved [40,41]. This last version is the one employed in this paper. The source maps obtained by EHR–CLEAN–SC (and the other CLEAN–SC versions) can be integrated by simply adding the powers of the deconvoluted *clean* sources calculated within a predefined region [42].
4. **Generalized inverse beamforming (GIBF)** [43,44] is an inverse method based on the eigenvalue decomposition of the CSM. Unlike direct beamforming methods, in which each potential source is assumed to be uncorrelated, GIBF takes into account the possible source interference by resolving all the sources at once. This makes it possible to resolve both correlated/uncorrelated sources as well as sparse and spatially–distributed sources. GIBF also requires the user to select the assumed number of eigenvalues to consider. Each eigenvalue represents the overall strength related to a coherent source distribution under the constraint of orthogonality. This method (with different regularization strategies) was recently applied to airfoil–noise measurements in open–jet wind tunnels [45–47]. In this paper, the regularization process recently proposed by Zamponi et al. [45,46] was employed. For the integration of the GIBF sound maps, the pressure values of each scanning grid point are summed and then squared due to the assumption of source coherence.

CFDBF was employed as a baseline reference to compare the other three more advanced methods to. The other three methods are state–of–the–art techniques and were selected for this analysis due to their expected good performance based on the literature [23,26]. In particular, FUNBF and EHR–CLEAN–SC are novel and, to the best knowledge of the authors, there are no publications reviewing the performance of these methods on aeroacoustic measurements, like the ones treated in this manuscript.

These methods were applied to three different experimental test cases featuring one speaker, two speakers, and airfoil trailing–edge noise measurements, respectively. The experiments featuring speakers were performed to have a known sound signal as a reference solution and to represent airframe noise experiments featuring multiple point sources such as landing gears [9], whereas obtaining accurate noise levels in trailing–edge noise measurements represents a typical challenge in aeroacoustic experiments [48]. The quality of the source maps obtained, the repeatability of the results and the source power estimations by the four methods are evaluated in this paper. The estimates for the source power of each method were compared to the reference signal, which is the average of all microphones of the array. In addition, for the case of the airfoil noise, the semi–empirical airfoil noise prediction method proposed by Brooks–Pope–Marcolini (BPM) [49] was also used for comparison.

It should be noted that removal of the main diagonal of the CSM [1,50], which is a method to neglect the contribution of the noise which is incoherent for all the array's microphones was not applied for any of the methods, since the microphone array was not in direct contact with the flow of the wind tunnel and the testing facility has low background noise levels.

More information about the characteristics of the test cases is included in section 2. Section 3 discusses the main results obtained for each method for all the test cases. Finally, the conclusions drawn are gathered in section 4.

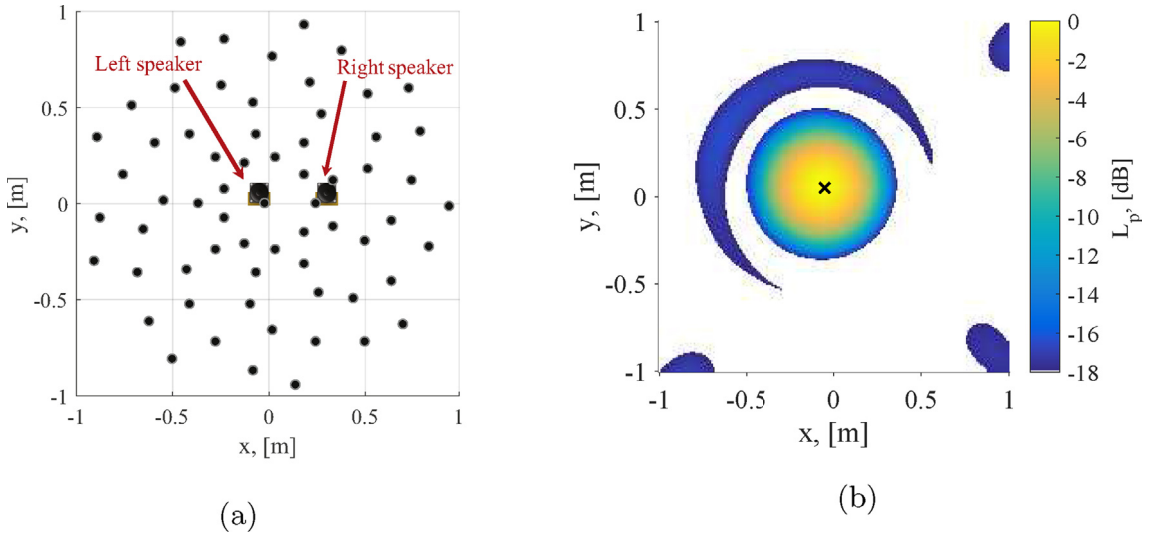

Fig. 1. (a) Scheme of the microphone distribution of the Array 1 (seen from behind) and relative position of the two speakers (situated 1 m away from the array's plane). (b) PSF of the Array 1 for a point source at the left speaker location (denoted by the black × symbol) emitting sound within a 630 Hz one–third–octave band.

2. Experimental setup

The experiments were performed in the anechoic vertical open–jet wind tunnel (A–tunnel) at Delft University of Technology [17,18,51], which is located in a room covered with wedges made of *Flamex Basic* acoustic absorbing foam [52] and has a cut–off frequency of 250 Hz, i.e., free–field conditions apply for higher frequencies. A microphone array consisting of 64 G R A.S. 40 PH analog free–field microphones [53] with integrated constant current power amplifiers was employed for all the experiments. All the microphones were calibrated in amplitude using a G.R.A.S. 42AA pistonphone [54], which emits a sinusoidal wave of 114 dB at 250 Hz. The relative phase responses of the microphones were also calculated employing a clapping device that generated an impulse broadband sound. This approach allows for the estimation of the difference in phase between the expected received signal and the actual recorded signal by each microphone, using the center microphone as reference. This calibration can be performed for all the frequencies of interest.

The microphone distribution employed for the measurements with speakers was optimized for a frequency range between 1 kHz and 10 kHz [40], see Fig. 1a, and provides an array diameter of approximately 2 m. This array is referred to as Array 1. In the same plot, the relative position of the two Visaton K 50 SQ speakers [55] used for the experiments can be observed. Each speaker was used for emitting a different, incoherent, synthetic broadband noise signal generated with MATLAB, see below. Both of them were situated at a distance of 1 m from the array plane and have a baffle diameter of approximately 45 mm. The (x, y, z) coordinates of the speakers (with the x and y axes centered at the array center microphone, see Fig. 1a, and the z axis normal to the array plane pointing towards the speakers) are (−0.05 m, 0.05 m, 1 m) for the left speaker and (0.3 m, 0.05 m, 1 m) for the right one. The test cases featuring speakers were performed without flow in the wind tunnel, i.e., simply using the facility as an anechoic chamber. The point spread function (PSF) [23] of this microphone array (Array 1) is shown in Fig. 1b for a point source located at the left speaker position emitting sound within a one–third–octave frequency band centered at 630 Hz.

For each measurement a sampling frequency of 50 kHz and 60 s of recording time were used. The acoustic data were averaged in time blocks of 8192 samples (giving a time block duration of 163.84 ms) and windowed using a Hanning weighting function with 50% data overlap, following Welch's method [56]. One–third–octave frequency bands will be used in the paper for comparison purposes. The frequency range of interest extended from 500 Hz to 5 kHz, which is typically the range considered for similar airfoil noise experiments [14–16,57].

For each test case, some considerations should be noted:

1. **Case I: Single speaker**. For the first test case, only the left speaker (see Fig. 1a) emitted sound. The same synthetic broadband noise signal was played at four different volumes, which provided four different signal to noise ratios (SNR) with respect to the background noise of the facility. These SNR values were calculated by subtracting the background noise spectrum of the wind–tunnel facility from the frequency spectrum of the speaker, all measured with the array (averaged over all microphones) and expressed in decibels. The background noise remained the same for all the cases involving speakers. The baseline pressure signal (SNR_1) was reduced in amplitude by a factor 10 (SNR_2), 50 (SNR_3) and 100 (SNR_4). For each SNR case, the signal was played ten times to investigate the repeatability of the results. For all cases, the average signal of all the microphones of the array was considered as the reference signal for comparison with the results of the four acoustic imaging methods. The signal of each microphone was corrected for expressing the sound level at 1 m from the sound source. For all methods, a scan grid going from $x = -1$ m to $x = 1$ m and from $y = -1$ m to $y = 1$ m was used, with $z = 1$ m and

spacing between grid points of $\Delta x = \Delta y = 0.01$ m. The obtained source maps were integrated over a square ROI centered at the left speaker (from $x = -0.15$ m to $x = 0.05$ m and from $y = -0.05$ m to $y = 0.15$ m, with $z = 1$ m), see the dashed squares in Fig. 4. The frequency spectra recorded by the array (averaged over all microphones) for all the SNR cases are presented in Fig. 2a, as well as the background noise (BGN) of the facility. The values shown are sound pressure levels L_p in decibels with a reference threshold pressure of 20 μPa. It is observed that an almost constant offset over the whole frequency range is obtained when decreasing the volume of the left speaker. These offsets have approximate values of −12 dB, −25 dB and −32 dB for SNR_2, SNR_3 and SNR_4, respectively, with respect to the maximum volume considered (SNR_1). It is also seen that the recorded signals for SNR_3 and SNR_4 collapse with the background noise spectrum of the facility for the lowest frequencies, which indicates that the speaker is emitting sound below the background noise in that frequency range, i.e., with a negative SNR. The sound spectra expected for those two SNR cases are depicted in red color in the same figure, assuming the aforementioned offset values of −25 dB and −32 dB, respectively.

2. **Case II: Two speakers**. For the case with two speakers, both speakers (left and right, see Fig. 1a) emitted sound simultaneously. The same synthetic broadband noise signal as in Case I was played by the left speaker with the volume of the SNR_1 case, and another different synthetic broadband noise signal (incoherent with the first signal) was played by the right speaker at four different volumes. The baseline signal for the right speaker is referred to as Volume 1. Volumes 2, 3 and 4 indicate cases with the right speaker emitting the signal of Volume 1 divided by a factor 4, 8, and 16, respectively. Additional recordings with just the right speaker were also performed, and the corrected averaged array signal was again taken as a reference. The challenge for this test case is to retrieve the correct signals emitted by each speaker, when both speakers are emitting simultaneously. The same scan grid was used as in Case I, as well as the ROI for the left speaker. The ROI for the right speaker spanned from $x = 0.2$ m to $x = 0.4$ m and from $y = -0.05$ m to $y = 0.15$ m, with $z = 1$ m, see the dashed squares in Fig. 9. The frequency spectra of the left speaker (SNR_1) and the right speaker (for the four different volumes) recorded by the array (averaged over all microphones) with only one of the speakers emitting sound at a time are plotted in Fig. 2b. Similarly as in Fig. 2a, an almost constant offset over the whole frequency range is obtained when decreasing the volume of the right speaker. These offsets have approximate values of −6 dB, −12 dB and −18 dB for Volumes 2, 3 and 4, respectively, with respect to Volume 1. These four volumes provide a wide range of ratios between the signals emitted by both speakers, having the right speaker from being the loudest source to being almost negligible compared to the left speaker. For this case, both speaker signals are stronger than the background noise of the facility.
3. **Case III: Airfoil trailing–edge noise**. A NACA 0018 airfoil was tested in the A–tunnel in order to investigate its turbulent boundary layer trailing edge (TBL–TE) noise emissions [1]. The wind tunnel has a contraction ratio of approximately 15 : 1 and was equipped with a rectangular test section of 0.4 m × 0.7 m. The airfoil was manufactured in aluminum and has a chord of 0.2 m and a span of 0.4 m, i.e., equal to the test section width. The airfoil was installed between two wooden plates of 1.2 m length, to approximate the two–dimensionality of the flow over most of the wing span [58], see Fig. 3c. Two freestream velocities V were considered for this paper: 20 m/s and 40 m/s, providing a maximum Mach number of 0.117 and a maximum chord–based Reynolds number of 5.27×10^5. Both velocities were uniform over the whole test section within 0.5% and with a turbulence intensity below 0.1% for the entire velocity range considered [17]. Since the maximum Reynolds number corresponds to the laminar regime, the transition to turbulent boundary layer was forced following the guidelines described in Ref. [59]. A tripping tape was used with carborundum elements with a nominal size of 0.84 mm,

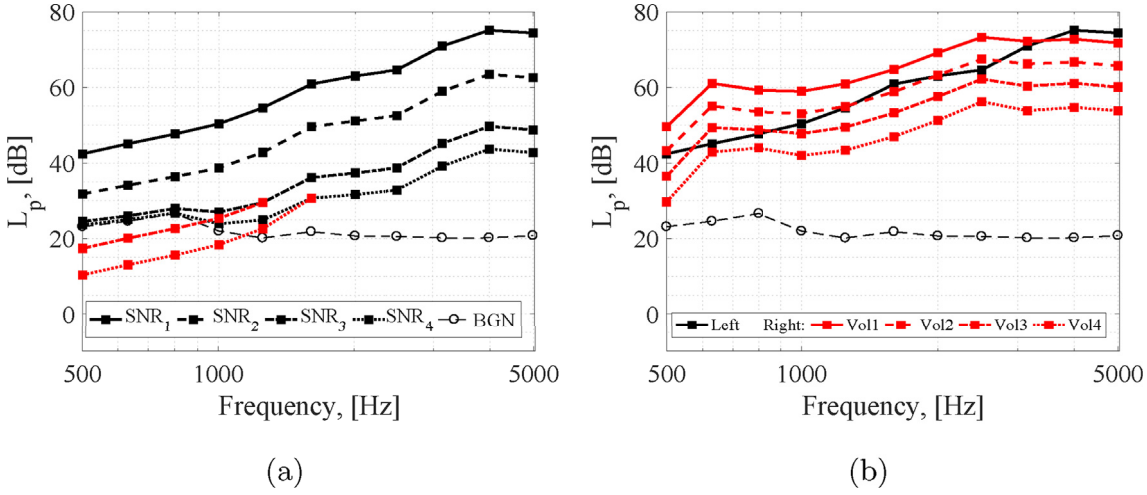

Fig. 2. One–third–octave band frequency spectra recorded by the array (averaged over all microphones) for: (a) The single speaker case for the four SNR cases. For SNR_3 and SNR_4 the predicted frequency spectra for the lower frequencies are depicted in red. (b) The case with two speakers for the four volumes of the right speaker (the signal of the left speaker with SNR_1 is also included for reference). The background noise spectrum (BGN) of the facility is also plotted in both graphs for reference. (For interpretation of the references to color in this figure legend, the reader is referred to the Web version of this article.)

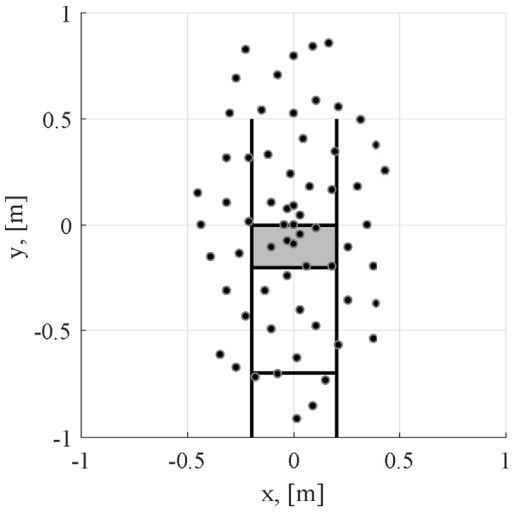

(a)

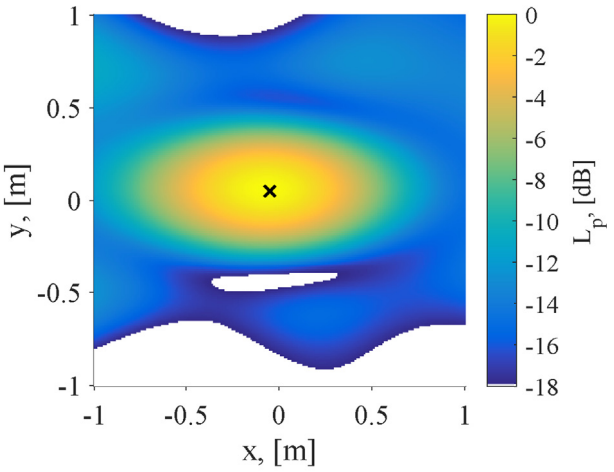

(b)

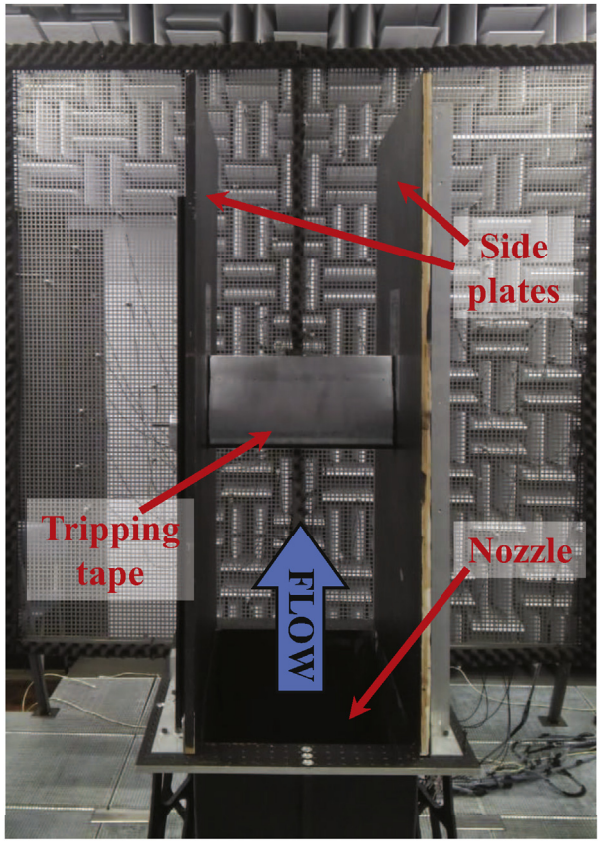

(c)

Fig. 3. (a) Scheme of the microphone distribution of the Array 2 (seen from behind) and relative position of the airfoil (depicted as a gray rectangle and situated 1.3 m away from the array's plane). The side plates and the nozzle's exit are indicated with solid black lines. (b) PSF of the Array 2 for a point source at the left speaker location (denoted by the black × symbol) emitting sound within a 630 Hz one–third–octave band. (c) Picture of the NACA 0018 airfoil between the side plates in the A-tunnel.

randomly distributed on a tape of 10 mm width, centered at 20% of the chord and covering the whole span on both sides of the airfoil, see Fig. 3c. The turbulent nature of the boundary layer was assessed using a remote wall–pressure probe. The

airfoil was set at a geometric angle of attack of $\alpha = 0°$ for all test cases using a digital angle meter [18]. The microphone distribution for the airfoil measurements corresponds to an adapted Underbrink spiral array design [60] with 7 spiral arms of 9 microphones each, and an additional microphone located at the center of the array. This design was scaled to half its size in the x direction, i.e., with approximate dimensions of 1 m × 2 m, for ensuring a clear sound propagation path from the airfoil's trailing to the microphones, limiting the blocking by the side plates, see Fig. 3a, and for separating the trailing–edge noise from other potential noise sources present in the y direction in an easier way. In the same plot, the relative position of the airfoil is depicted as a gray rectangle. This array is referred to as Array 2. The corresponding PSF [23] is illustrated in Fig. 3b, also for a point source located at the left speaker position (for comparison purposes with Fig. 1b) emitting sound within a one–third–octave frequency band centered at 630 Hz. It is observed that this PSF is more elongated in the x direction due to the smaller aperture of the array in that direction. The airfoil trailing edge was located at a distance of $z = 1.3$ m from the array plane and the center of the trailing edge was approximately aligned with the center microphone of the array ($x = 0$ m and $y = 0.05$ m). The airfoil leading edge was situated 0.5 m above the outlet of the wind–tunnel nozzle to separate potential extraneous noise sources coming from the nozzle. The signal measured by the array (averaged over all microphones) was again considered as a reference, as well as the predictions by the BPM model. It should be noticed that both the averaged microphone signals and the BPM model consider the noise emissions of the whole airfoil and not just the trailing–edge noise, which is the object of interest of this study. The averaged microphone measurements also includes the background noise of the wind–tunnel facility. For all methods a scan grid ranging from $x = -0.5$ m to $x = 0.5$ m and from $y = -0.5$ m to $y = 0.5$ m was used, with $z = 1.3$ m and a spacing between grid points of $\Delta x = 0.01$ m. The obtained source maps were integrated within a rectangular ROI spanning from $x = -0.1$ m to $x = 0.1$ m and from $y = 0$ m to $y = 0.1$ m, with $z = 1.3$ m, see dashed rectangles in Figs. 13 and 14.

3. Results discussion

3.1. Case I: single speaker

3.1.1. Source maps

Figure 4 presents one example source map obtained by each of the four methods considered for the single speaker case, with the lowest SNR (SNR_4). The results correspond to a one–third–octave frequency band centered at 630 Hz and all maps have the same dynamic range of 18 dB. This frequency band was selected because it represents one of the lowest SNR cases, see Fig. 2a. The speaker signal for this frequency band is even lower than the background noise, i.e., it has a negative SNR value (about −11.5 dB).

The CFDBF source map is depicted in Fig. 4a and it is observed that, apart from the speaker (located approximately in the center of the plot), there are two other dominant noise sources: one at the top of the map (approximately at $x = 0.1$ m and $y = 1$ m) and another one at the bottom left corner of the map (approximately at $x = -1$ m and $y = -1$ m). The analysis of a recording of the background noise indicated that these two sources are indeed real and part of the background noise of the wind tunnel facility, rather than being sidelobes. Apart from that, the results obtained with CFDBF show a poor spatial resolution and a high sidelobe level (about 8 dB lower than the peak level). The source map provided by FUNBF (Fig. 4b) shows a similar source distribution as the CFDBF map but with narrower main lobes and lower sidelobe level (about 12 dB lower than the peak level). EHR–CLEAN–SC (Fig. 4c) shows main lobes with a width selected by the user. There seems to be a *floor* on this source map between 0 dB and 2 dB, which indicates that there are still remaining contributions to the CSM of the *dirty* map, after subtracting the contribution of the identified sound sources. The two aforementioned background noise sources are detected as discrete point sources. This example highlights the importance of selecting a conservative number of expected sound sources for EHR–CLEAN–SC (three in this case) by observing the CFDBF source map and verifying the number of dominant eigenvalues in the CSM. If only one source is considered, only the noise source at the bottom left of the map would be identified since it is the strongest source. Lastly, GIBF (Fig. 4d) seems to provide the cleanest results from the four methods, showing the correct source location with no other secondary sources or sidelobes. This is because only the third largest eigenvalue (corresponding to the speaker) was selected for plotting. The peak levels of GIBF, however, are considerably lower than for the other three methods since it is difficult to directly relate the peak levels of this technique to the actual source intensity of each grid point. The reason for this difficulty is in the different output provided by inverse methods. Whereas CFDBF, FUNBF and EHR–CLEAN–SC indicate the peak source intensity, GIBF maps display the source distribution contours, which should be integrated, considering the assumption of source coherence as explained in section 1, in order to be compared with the peak levels computed by the other methods. This procedure was done when calculating the frequency spectra, see section 3.1.2 below.

3.1.2. Frequency spectra

The sound spectra obtained by each method by integrating the source maps within the ROI are shown in Fig. 5 for all cases. The source maps obtained by CFDBF were integrated using the source power integration (SPI) method [25,32,33]. The maps obtained by FUNBF were integrated using an adapted version of SPI for considering the FUNBF formulation [8,9].

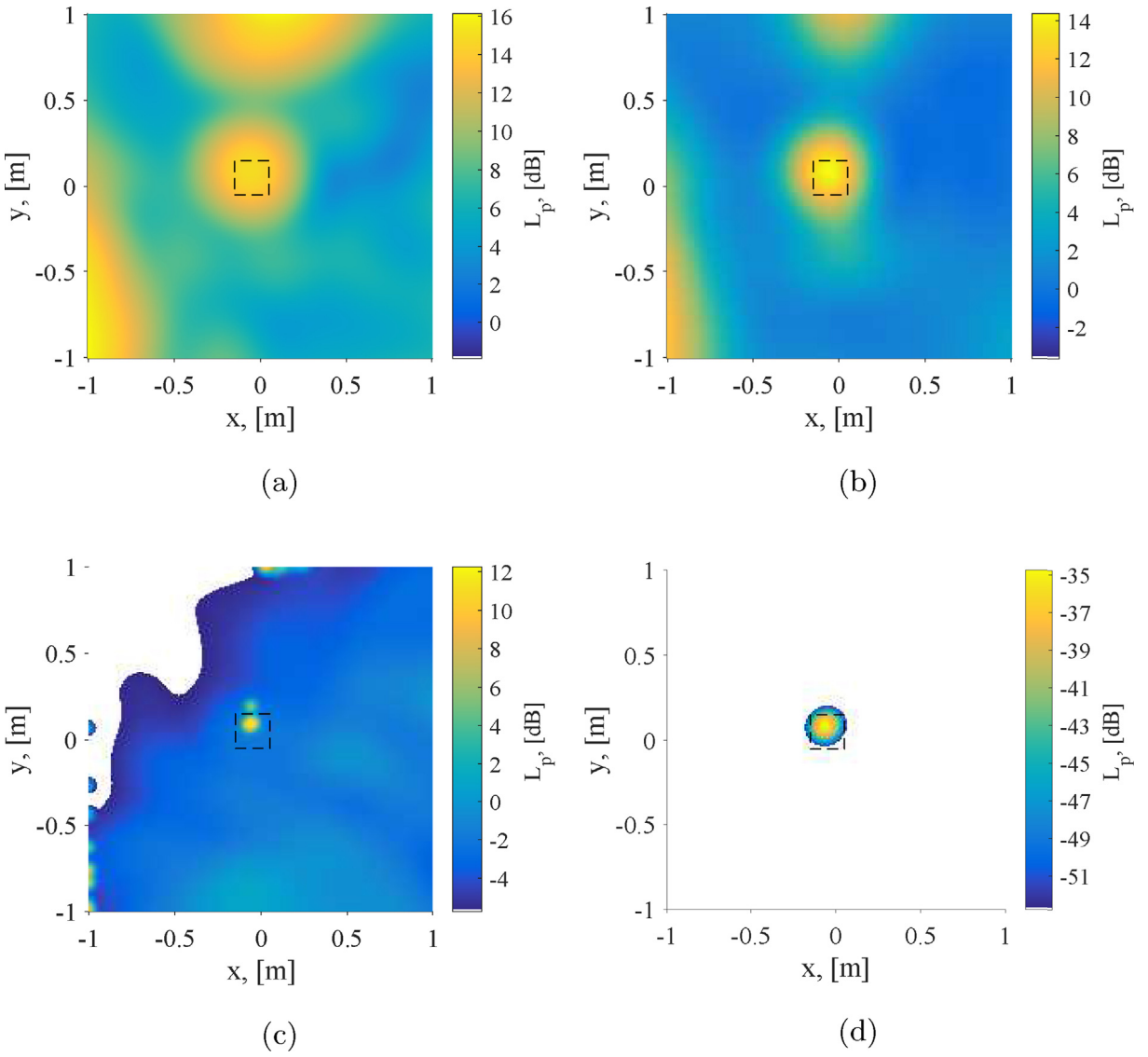

Fig. 4. Source maps for the case of a single speaker with the lowest SNR (SNR_4) for a one–third–octave frequency band centered at 630 Hz for: (a) CFDBF, (b) FUNBF with $\nu = 8$, (c) EHR–CLEAN–SC, and (d) GIBF. The dashed squares denote the ROI.

For clarity reasons, only the averaged spectra over the ten repetitions are plotted. The reference averaged array signal is also shown, as well as the background noise spectrum of the facility. For the first two SNR cases (Fig. 5a and b) all the methods provide a close match with respect to the reference averaged array signal, except for FUNBF at higher frequencies (4 and 5 kHz). This decay is most likely caused by the sensitivity of this method to a mismatch in the steering vector, which occurs when a coarse grid is employed [4,5,35,61] and the positions of the grid points do not coincide exactly with the source locations. This is an increasingly important source of errors for high frequencies or high values of the exponent ν.

When the SNR of the speaker is lowered even more (Fig. 5c and d), the sound from the speaker is below the background noise of the facility for some frequency bands (approximately below 1 kHz), i.e., it has a negative SNR. For those frequency bands, all the acoustic imaging methods considered provide values below the background noise but with a larger spread between the different methods. The aforementioned decay at high frequencies for FUNBF remains similar for the four different SNR cases.

In order to assess the accuracy in retrieving the correct sound spectra, the relative errors made by each method with respect to the reference average microphone signal $\Delta L_p = L_{p,method} - L_{p,ref}$ were calculated. A positive value of ΔL_p corresponds to an overprediction of the result by the acoustic imaging method and vice versa. For calculating ΔL_p, the averaged spectra over the ten repetitions were employed. The relative errors are plotted in Fig. 6 for all the SNR cases. For the two lowest SNR cases (SNR_3 and SNR_4) the errors below a threshold frequency of 1 kHz and 1.25 kHz, respectively, were considered with respect to the predicted frequency spectra below the background noise, see lines in red color in Fig. 2a. In addition, the absolute error made

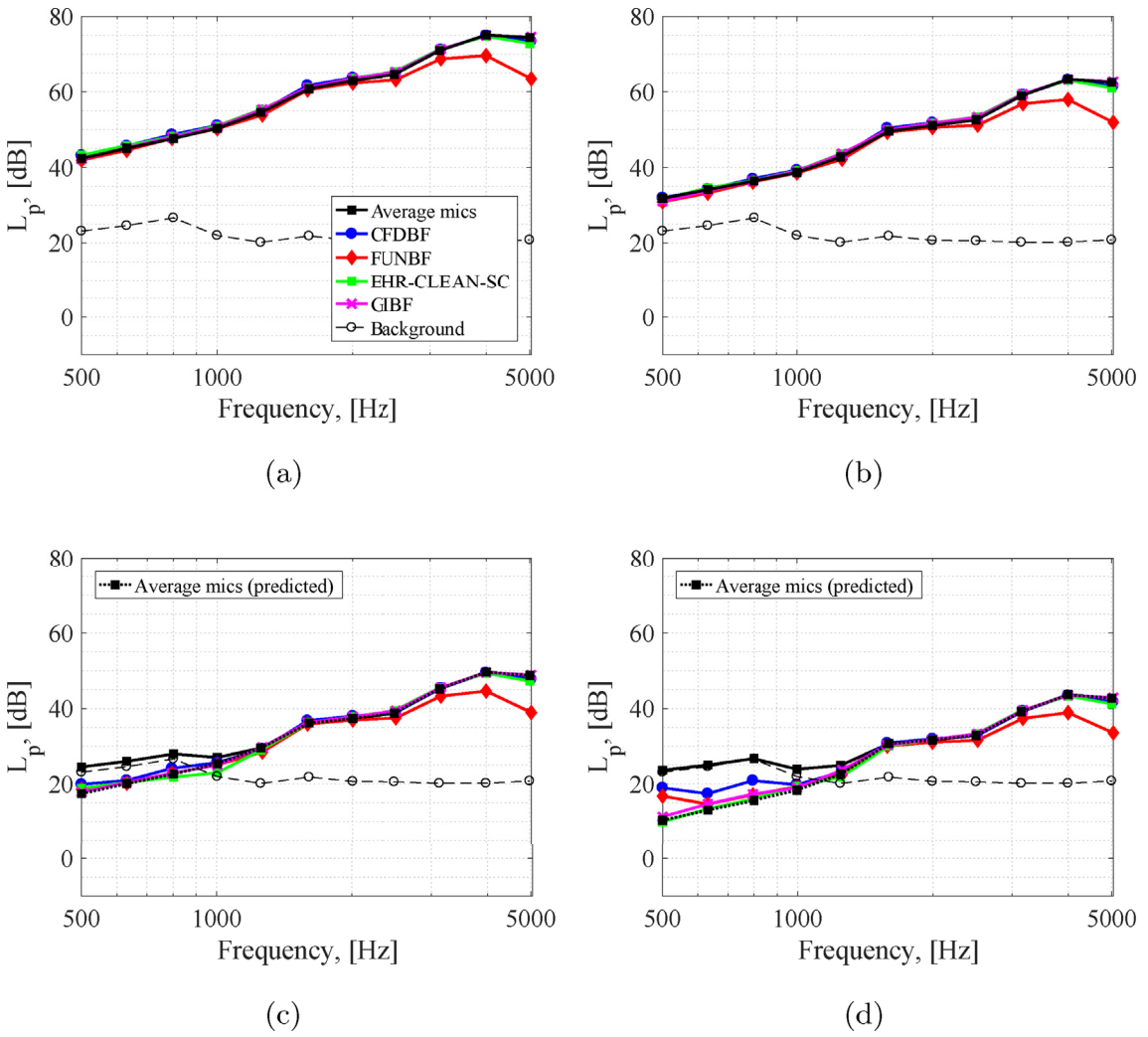

Fig. 5. Averaged one–third–octave band frequency spectra for all the considered acoustic imaging methods, as well as for the average microphone signal and the background noise of the facility for the case of a single speaker with: (a) SNR_1, (b) SNR_2, (c) SNR_3, and (d) SNR_4.

by each method averaged over the whole frequency range considered (the eleven one–third–octave bands) $\epsilon = \overline{|\Delta L_p|}$ (i.e., the average $\mathcal{L}^1$ norm of the differences) is also calculated and included in the legends of Fig. 6.

For the first two SNR (Fig. 6a and b) the ΔL_p values are contained within ± 1 dB for the four methods for most frequencies, except for the aforementioned decay at high frequencies for FUNBF that reaches maximum errors of about 11 dB at the 5 kHz band. Except for FUNBF, the other three methods show a comparable performance for the first three SNR cases, with ϵ values up to 0.8 dB. For the lowest SNR case (SNR_4, Fig. 6d) the errors made by each method increase for low frequencies, where the SNR of the speaker is lowest, especially for CFDBF and FUNBF which seem to be influenced by the presence of the background noise sources.

It is observed that, in general, GIBF provides the lowest overall error with respect to the reference signal with ϵ values below 0.7 dB, followed closely by EHR–CLEAN–SC with $\epsilon \leq 0.8$ dB. CFDBF provides almost the same results as EHR–CLEAN–SC except for SNR_4, where it provides considerably higher estimates at low frequencies (and ϵ increases to 2 dB). Lastly, FUNBF offers relatively good results for low and mid frequencies, but the considerable decay at high frequencies causes ϵ values up to 2.6 dB. It also presents errors of about 6 dB at the 500 Hz band for the lowest SNR case. As aforementioned, the errors made by FUNBF for high frequencies can be reduced by using a finer grid, which would increase the computational time of the processing. This is shown in Fig. 7 which shows the FUNBF results for the SNR_1 case using grids with a spacing between grid points $\Delta x = \Delta y$ of 5 mm and 1 mm, respectively. Finer grids reduce the errors considerably but the previous grid (with $\Delta x = \Delta y = 10$ mm) was used for a fair comparison with other methods throughout the paper.

A summary of all the ϵ values for each method and each SNR case is included in Table 1.

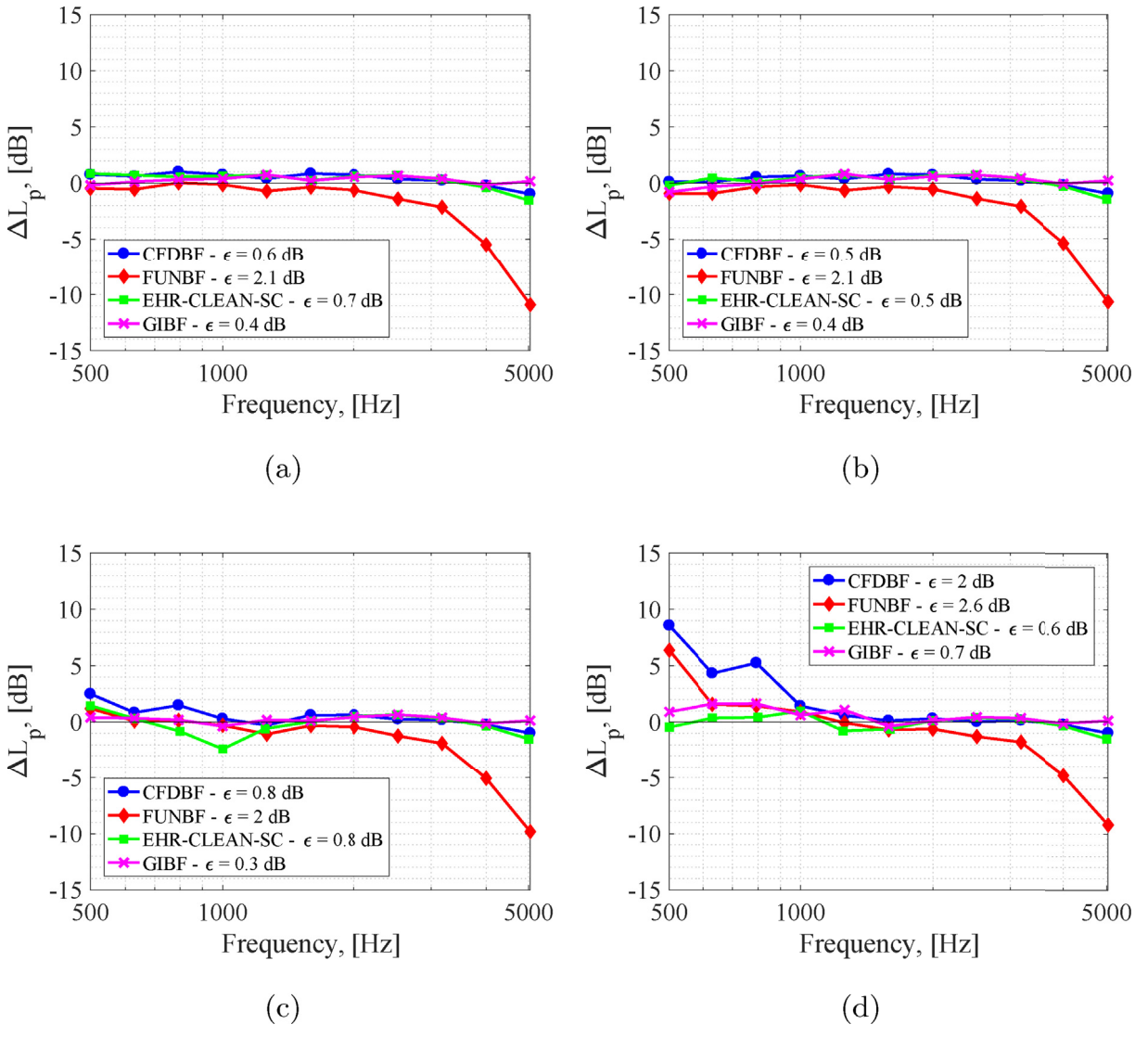

Fig. 6. Average error per third–octave band made by each acoustic imaging method, with respect to the average microphone signal for the case of a single speaker with: (a) SNR_1, (b) SNR_2, (c) SNR_3, and (d) SNR_4.

Table 1
Absolute errors made by each method averaged over the whole frequency range (ϵ, in dB) with respect to the average microphone signal for the experiment with a single speaker.

Case	CFDBF	FUNBF	EHR–CLEAN–SC	GIBF
SNR_1	0.6	2.1	0.7	0.4
SNR_2	0.5	2.1	0.5	0.4
SNR_3	0.8	2	0.8	0.3
SNR_4	2	2.6	0.6	0.7

3.1.3. Repeatability of the results

The repeatability of the results of each method was investigated considering the ten repetitions recorded for each SNR case. Fig. 8 depicts the standard deviation s (in decibels and per third–octave–band) of the estimated from each method, as well as the standard deviation of the reference signal of the array (averaged over all microphones). This latter is caused by small perturbations in the non–perfect measurement environment and the intrinsic uncertainties of the microphone and the speaker.

In general, most s values are below 0.2 dB for the highest SNR and become lower as the SNR decreases, reaching values about 0.05 dB for the $SNR_{left,4}$ case (Fig. 8d). Overall, the standard deviations of all methods collapse almost perfectly with those of the

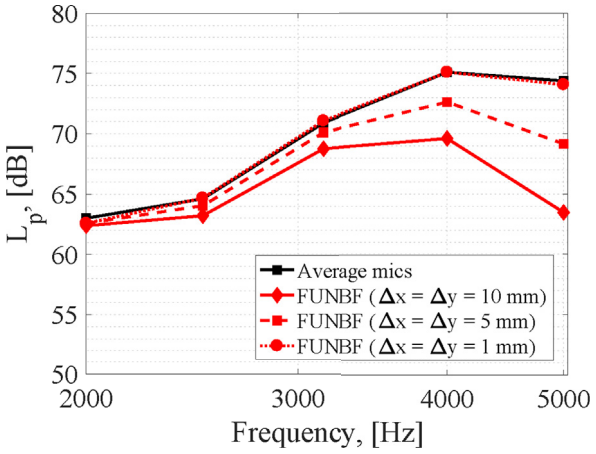

Fig. 7. Influence of the grid fineness in the results of FUNBF (with $\nu = 8$) for the case of a single speaker with SNR_1.

array center microphone, meaning that the deviations in the results are because of the nature of the recorded signals themselves and not due to a lack of robustness in the acoustic imaging methods. Only a few exceptions stand out in Fig. 8.

- The first one is the higher value of s for FUNBF at 5 kHz in Fig. 8a, which is most likely due to the aforementioned sensitivity to mismatch of this method at high frequencies.
- Secondly, in Fig. 8c, EHR–CLEAN–SC shows considerably larger deviations ($s \leq 0.35$ dB) for 800 Hz and 1 kHz. Lastly, for the lowest SNR case (Fig. 8d) this method reaches s values of about 0.75 dB for the 500 Hz band. These exceptions are located in the frequency range where the SNR is negative, see Fig. 2a. Through a careful investigation of the source maps produced by EHR–CLEAN–SC at the lowest SNR case at 500 Hz, where s is the highest, it was found that the strongest source of noise is the background noise, similar to the behavior seen in Fig. 4. The identified number and location of those background noise sources vary among the different repetitions. The CLEAN–SC–based algorithms work from the stronger (higher L_p) to the weaker source (lower L_p). Therefore, when the level of the strongest source varies, the information left after *cleaning* the map for identifying the remaining weaker sources (including the speaker in this case) will also vary. This fact likely causes the larger variation in the resolved speaker's sound pressure levels.
- Lastly, for the 500 Hz band, GIBF also shows a higher variability with $s \approx 0.4$ dB, which may depend on the presence of noise sources extraneous to the scanning grid plane due to the dominant background noise. Indeed, this inverse algorithm reconstructs the external noise source distributions recorded by the microphones through the generation of non–negligible amplitudes concentrated around the border of the grid plane. This edge effect reduces the accuracy of the source intensity estimation and, therefore, it increases its variability, when the $\mathcal{L}^1$ norm approach is adopted [43] since the sparsity of the solution is higher in this case. Increasing the extension of the scanning grid plane may represent a possible solution to improve the GIBF results at low frequencies with a negative SNR, with the consequent increase of the computational time required.

3.2. Case II: two speakers

3.2.1. Source maps

Fig. 9 contains one example source map obtained by each of the methods considered for the case with two speakers with the lowest volume in the right one (Volume 4). These results also correspond to a one–third–octave frequency band centered at 630 Hz. This frequency band was selected because for the given array geometry and distance between sources (0.35 m), it approximately represents the Rayleigh resolution limit frequency ($\sim$ 645 Hz) for which the two sources can be distinguished using conventional acoustic imaging methods. The sound pressure levels emitted by both speakers are practically identical for these conditions, see Fig. 2b.

The source map obtained by CFDBF (Fig. 9a) shows an elongated sound source with a peak between the actual positions of both speakers, due to the insufficient spatial resolution of this method for this frequency, as mentioned above. There are still some sidelobes present in the source map, about 14 dB lower than the peak level. FUNBF (Fig. 9b) removes the sidelobes from the CFDBF source map and just distinguishes both speakers as separate sound sources. Distinguishing both sources becomes easier if the exponent parameter ν of this method is increased, at the risk of stronger instabilities at high frequencies [5]. EHR–CLEAN–SC (Fig. 9c) performs best for this case showing virtually no sidelobes and clearly separating both speakers with the correct L_p levels. Lastly, the results obtained by GIBF (Fig. 9d) depict a somehow distributed line source with maximum levels at both ends of the segment, slightly further away than the actual positions of the speakers. Once again, it is not straightforward to relate the peak levels in the GIBF source map to the actual source intensity due to the different output provided by this method.

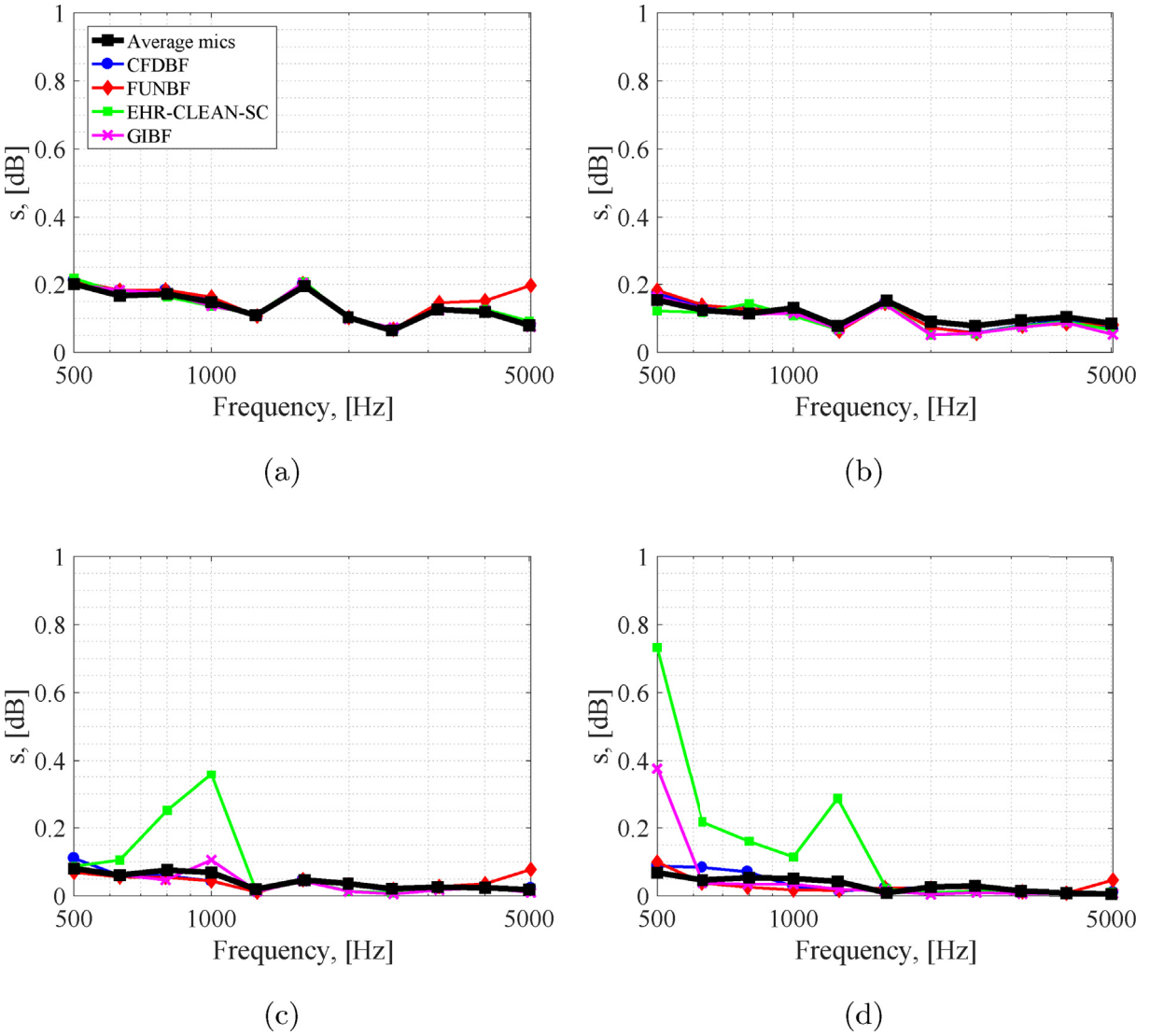

Fig. 8. Standard deviation s for all the considered acoustic imaging methods, as well as for the signal recorded by the array (averaged over all microphones) for the 10 repetitions for each one–third–octave band for the case of a single speaker with: (a) SNR_1, (b) SNR_2, (c) SNR_3, and (d) SNR_4.

3.2.2. *Frequency spectra*

In a similar way as it was done for the single speaker case, the integrated spectra within the two ROIs depicted in Fig. 9 were compared, respectively, to the reference signals of the left and right speaker recorded by the array and averaged over all microphones and corrected for the distance of 1 m to the sound source (with only one speaker emitting in that case).

As explained in section 2, the left speaker was set to emit the exact same synthetic broadband noise signal as in the SNR_1 case (i.e., same L_p values) and the right speaker emitted the same signal at four different volumes. Fig. 10 presents the resulting average one–third–octave band spectra for the left speaker. The Rayleigh resolution limit for the given setup ($\sim$ 645 Hz) is also denoted as a vertical dotted black line in all the plots of Figs. 10 and 11. The spectra of the left speaker (for the four right speaker volumes) are shown in the left column (Fig. 10a, c, 10e and 10g), whereas the respective relative errors ΔL_p with respect to the reference signal are presented in the right column (Fig. 10b, d, 10f and 10h). It is important to note that the volume of the left speaker is kept the same. As a general trend, the average absolute errors ϵ made by the four methods decrease when the volume of the right speaker decreases, as expected. In general, GIBF shows the best results for this case (with $\epsilon \leq 0.5$ dB). The second best method is EHR–CLEAN–SC (with $\epsilon \leq 1.6$ dB) which presents a similar behavior as GIBF but with some higher errors at lower frequencies, especially for the higher volume cases. CFDBF and FUNBF show a consistent large overestimation of the levels for the lower part of the frequency range, with the additional decay at high frequency for FUNBF. CFDBF makes average errors of $\epsilon \approx 3.8$ dB whereas for FUNBF it increases up to $\epsilon \approx 5$ dB.

Fig. 11 contains the obtained spectra for the right speaker (Fig. 11a, c, 11e and 11g). The right column depicts ΔL_p with respect to the reference signal (Fig. 11b, d, 11f and 11h). In this case, the errors increase when decreasing the volume of the right

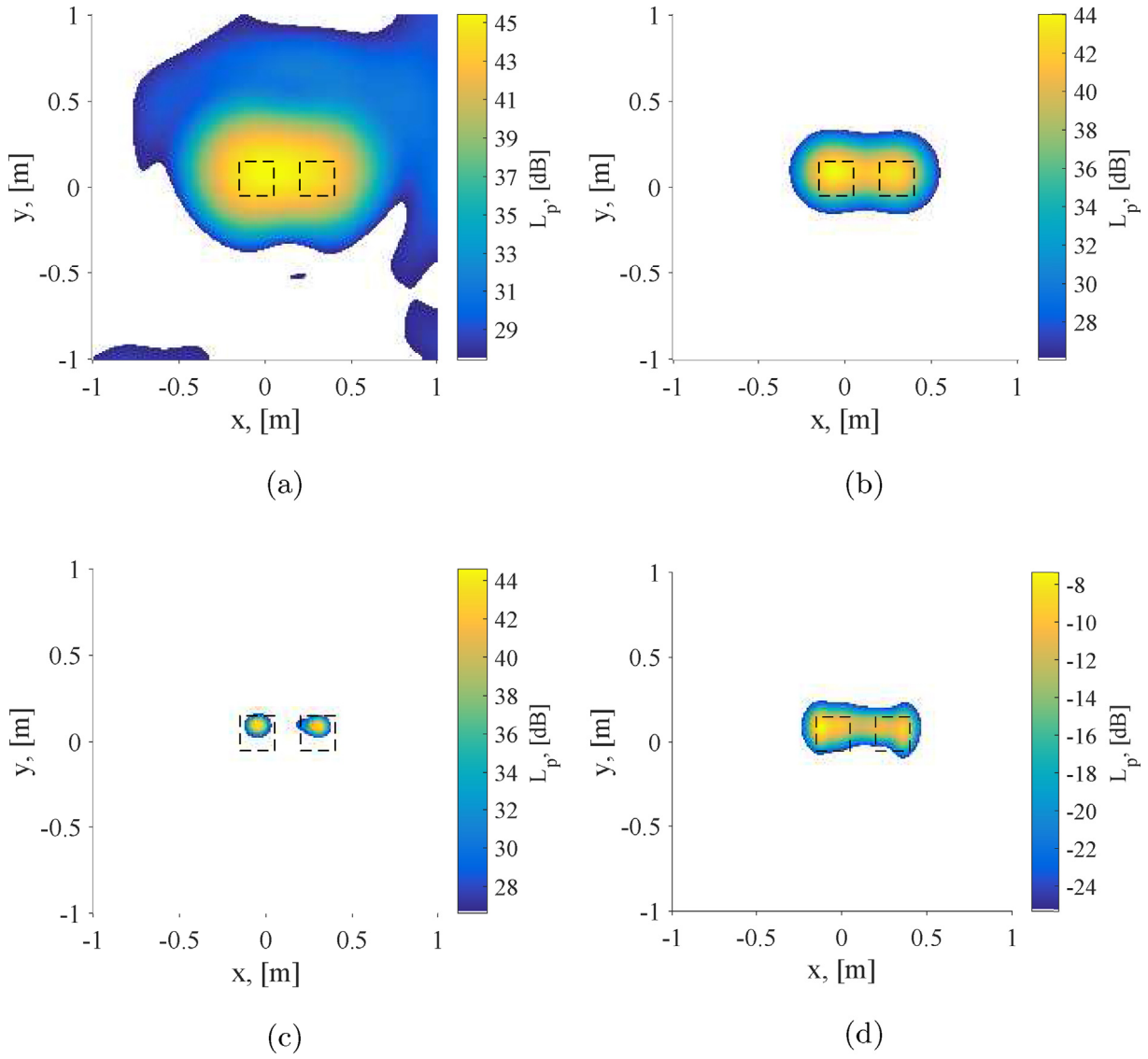

Fig. 9. Source maps for the case of two speakers with the right speaker emitting with the lowest volume (Volume 4) for a one–third–octave frequency band centered at 630 Hz for: (a) CFDBF, (b) FUNBF with $\nu = 8$, (c) EHR–CLEAN–SC, and (d) GIBF. The dashed squares denote the ROIs.

speaker. This is expected, since, when decreasing the volume, the right speaker becomes less dominant compared to the left speaker. Once again, GIBF seems to make the smallest errors for this case (with $\epsilon \leq 1.2$ dB) followed closely by EHR–CLEAN–SC (with $\epsilon \leq 2.1$ dB). Both methods show no anomalies, except for a considerable decay at high frequencies for EHR–CLEAN–SC for the case with volume 3. The performance of CFDBF and FUNBF is quite similar for all cases (with FUNBF making slightly larger errors), except for volume 4, where CFDBF shows a large overestimation of the results at high frequencies. This is due to the relatively low levels emitted by the right speaker in comparison with the left speaker for that frequency range (about than 20 dB lower), see Fig. 2b. In fact, observing the source maps at those frequencies (not included in this paper), the sidelobes due to the presence of the left speaker are stronger than the right speaker, and those sidelobes are included in the integration of the ROI.

All values of ϵ for the experiment featuring two speakers are included in Table 2.

3.3. Case III: airfoil trailing–edge noise

3.3.1. Signal to noise ratio (SNR)

The SNR values for the NACA 0018 airfoil experiment for both flow velocities (20 m/s and 40 m/s) are presented in Fig. 12. These SNR values were calculated by subtracting the background noise spectrum of the wind–tunnel facility at the corresponding velocity from that measured with the airfoil present. All cases were measured with the array (averaged over all microphones)

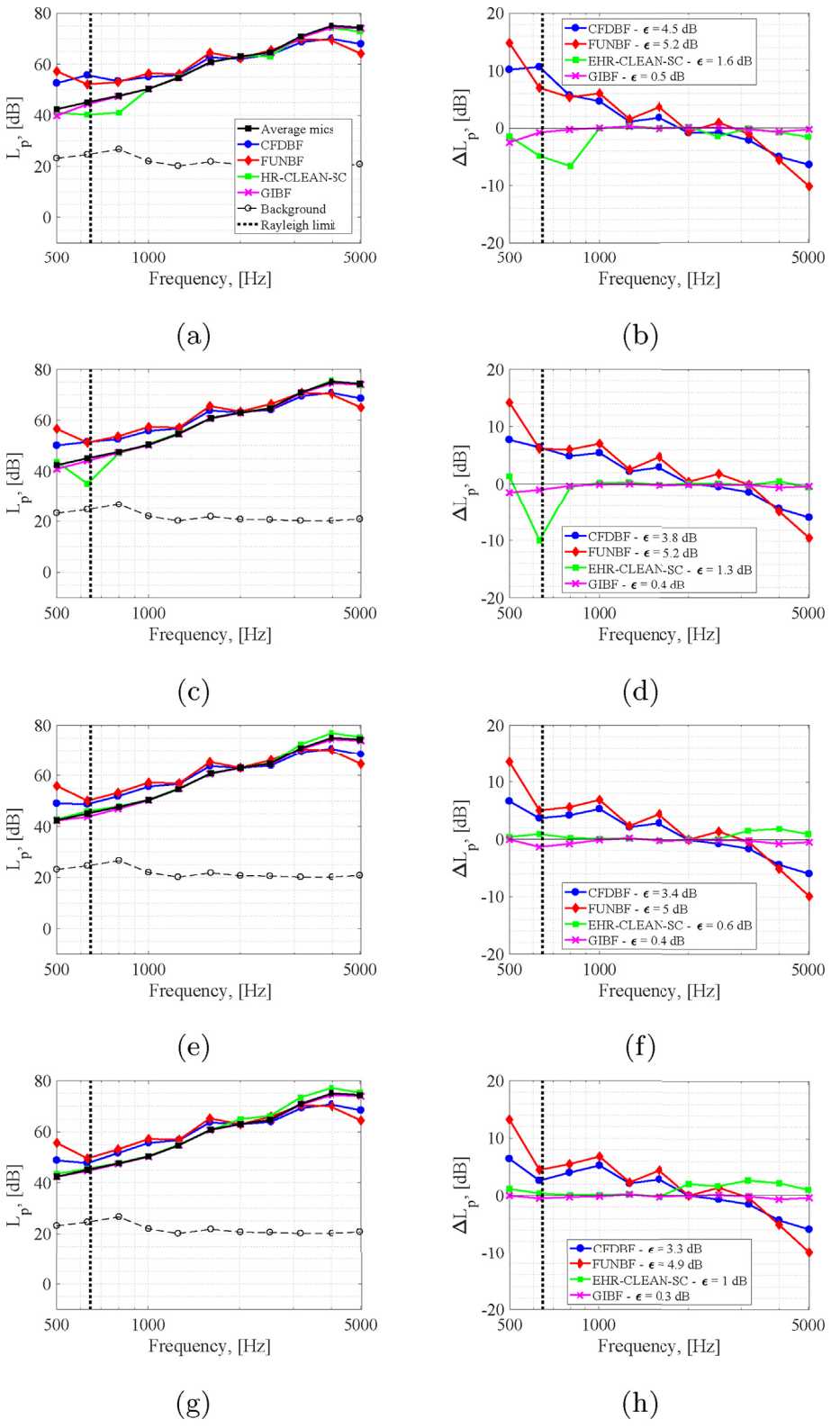

Fig. 10. Left column: Averaged spectra for the left speaker (with both speakers on) for all the considered acoustic imaging methods, as well as for the average array signal (with only the left speaker on) and the background noise. Right column: Average error made by each acoustic imaging method, with respect to the average array signal. The rows refer to different volumes set in the right speaker (from Volume 1 in the top to Volume 4 in the bottom). The frequency corresponding to the Rayleigh resolution limit (~ 645 Hz) is plotted as a dotted vertical line.

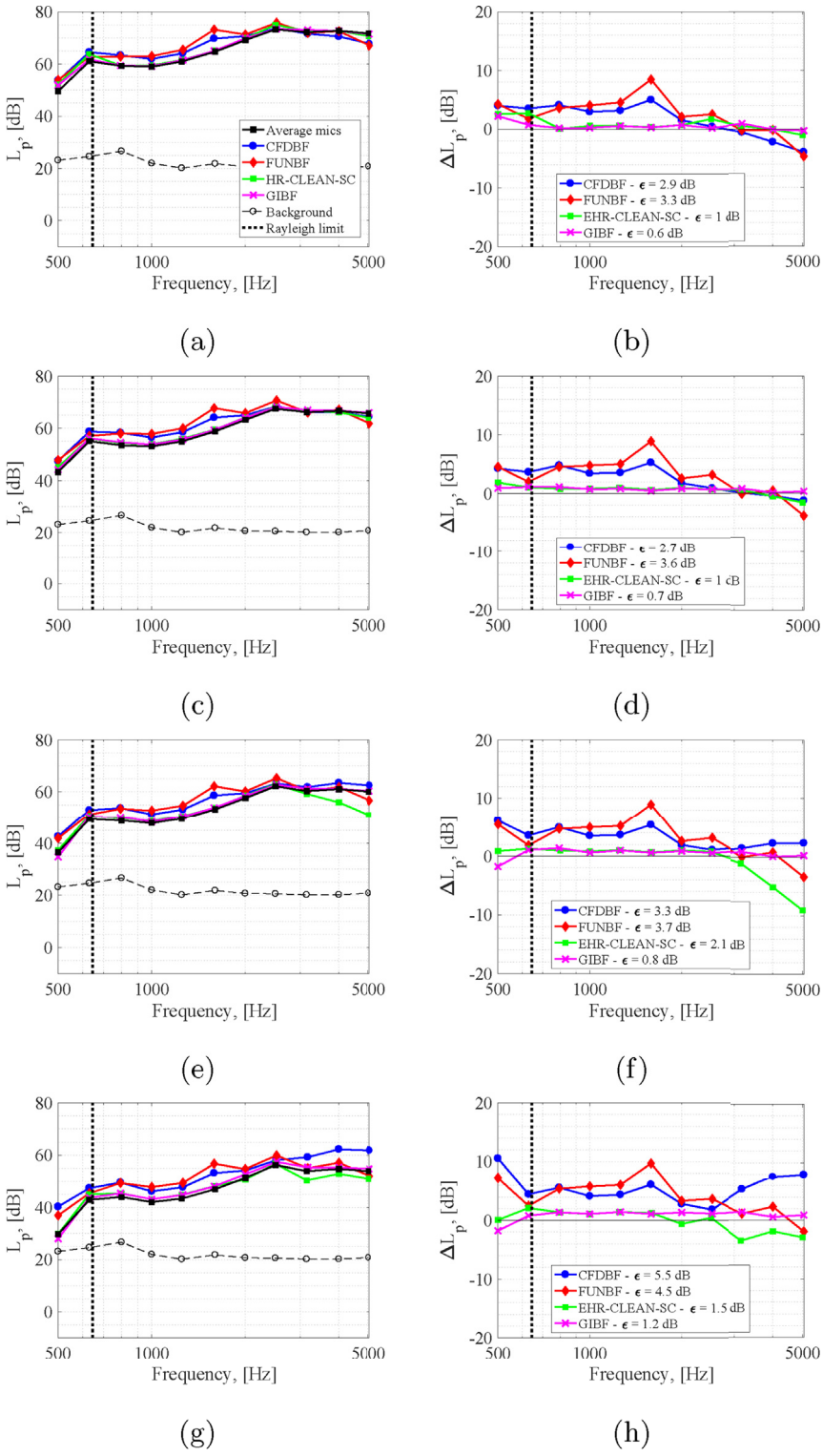

Fig. 11. Left column: Averaged spectra for the right speaker (with both speakers on) for all the considered acoustic imaging methods, as well as for the average array signal (with only the right speaker on) and the background noise. Right column: Average error made by each acoustic imaging method, with respect to the average array signal. The rows refer to different volumes set in the right speaker (from Volume 1 in the top to Volume 4 in the bottom). The frequency corresponding to the Rayleigh resolution limit ($\sim$ 645 Hz) is plotted as a dotted vertical line.

Table 2
Absolute errors made by each method averaged over the whole frequency range (ϵ, in dB) with respect to the average array signal for the experiment with two speaker.

Case	CFDBF	FUNBF	EHR–CLEAN–SC	GIBF
Left speaker – Volume 1	4.5	5.2	1.6	0.5
Left speaker – Volume 2	3.8	5.2	1.3	0.4
Left speaker – Volume 3	3.4	5	0.6	0.4
Left speaker – Volume 4	3.3	4.9	1	0.3
Right speaker – Volume 1	2.9	3.3	1	0.6
Right speaker – Volume 2	2.7	3.6	1	0.7
Right speaker – Volume 3	3.3	3.7	2.1	0.8
Right speaker – Volume 4	5.5	4.5	1.5	1.2

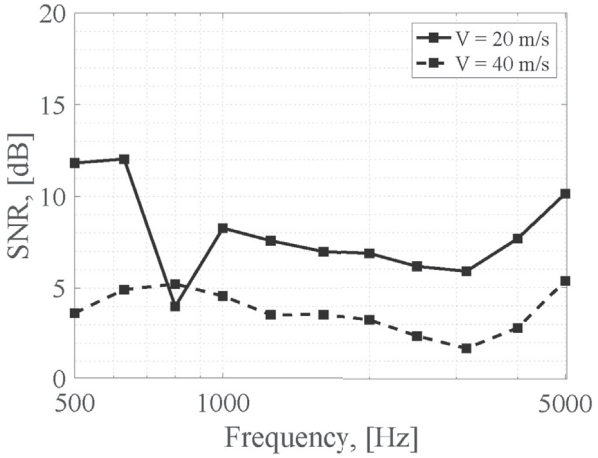

Fig. 12. SNR values considering the average array signal for each one–third–octave band for the NACA 0018 airfoil and flow velocities of 20 m/s and 40 m/s, respectively.

and expressed in decibels. Interestingly, the SNR decreases when the flow velocity increases, indicating that the background noise levels of the wind tunnel increase with the flow velocity faster than those from the airfoil. The unexpectedly low SNR value for the $V = 20$ m/s case at 800 Hz is due to the presence of tonal noise in the wind tunnel system that only occurs at that flow velocity and frequency band. For $V = 20$ m/s the average SNR is approximately 7.5 dB, whereas for $V = 40$ m/s it has a value of about 3.5 dB. It is observed that there is a positive SNR for both cases over the whole frequency range.

3.3.2. Source maps

Two sets of source plots for the NACA 0018 airfoil are presented in Figs. 13 and 14 for illustration purposes. All the maps have the same dynamic range (12 dB).

The first case corresponds to a flow velocity of 40 m/s and a one–third–octave frequency band centered at 1 kHz. The CFDBF source plot (Fig. 13a) depicts a distributed sound source along the trailing edge, but also extraneous noise sources coming from the collector and the nozzle of the wind tunnel, located at the top and the bottom of the picture, respectively. FUNBF (Fig. 13b) improves the results to some extent by narrowing the width of the line source at the trailing edge and separating the extraneous noise sources slightly further. EHR–CLEAN–SC (Fig. 13c) provides a cluster of sound sources somewhat distributed in the vicinity of the trailing edge and mostly concentrated in the middle of the edge, with lower strengths than the results from CFDBF and FUNBF. The extraneous noise sources are basically eliminated but few additional point sources are unexpectedly found upstream of the trailing edge (at about 60% of the airfoil chord). Finally, GIBF (Fig. 13d) shows a slightly elongated sound source located at the center of the trailing edge, without any other sound sources present. As aforementioned, it is not straightforward to relate the peak levels in the GIBF source map to the actual source intensity due to the different output provided by this method, see section 3.1.

The second example refers to the other flow velocity (20 m/s) and a one–third–octave frequency band centered at 4 kHz. These conditions were selected because the contribution of the leading–edge noise was observed to be dominant compared to the trailing–edge noise. The increased relevance of leading–edge noise at high frequencies was also observed in a similar experiment featuring a tripped NACA 63–215 Mod–B airfoil by Bahr et al. [48]. In that experiment, however, the airfoil chord was double (0.4 m), the flow velocity was almost three times higher ($M = 0.17$) and the frequency considered also about three times higher (12.5 kHz) compared to the results shown in Fig. 14. The exact cause for having the leading edge noise as a dominant source at the conditions of the current experiment is not known with certainty yet since this type of source is normally generated due to the incoming turbulence of the flow [49] and the turbulence intensity levels for the wind tunnel used are below 0.1%. A possible cause of this noise source could be the tripping tape mentioned in section 2, placed at 20% of the

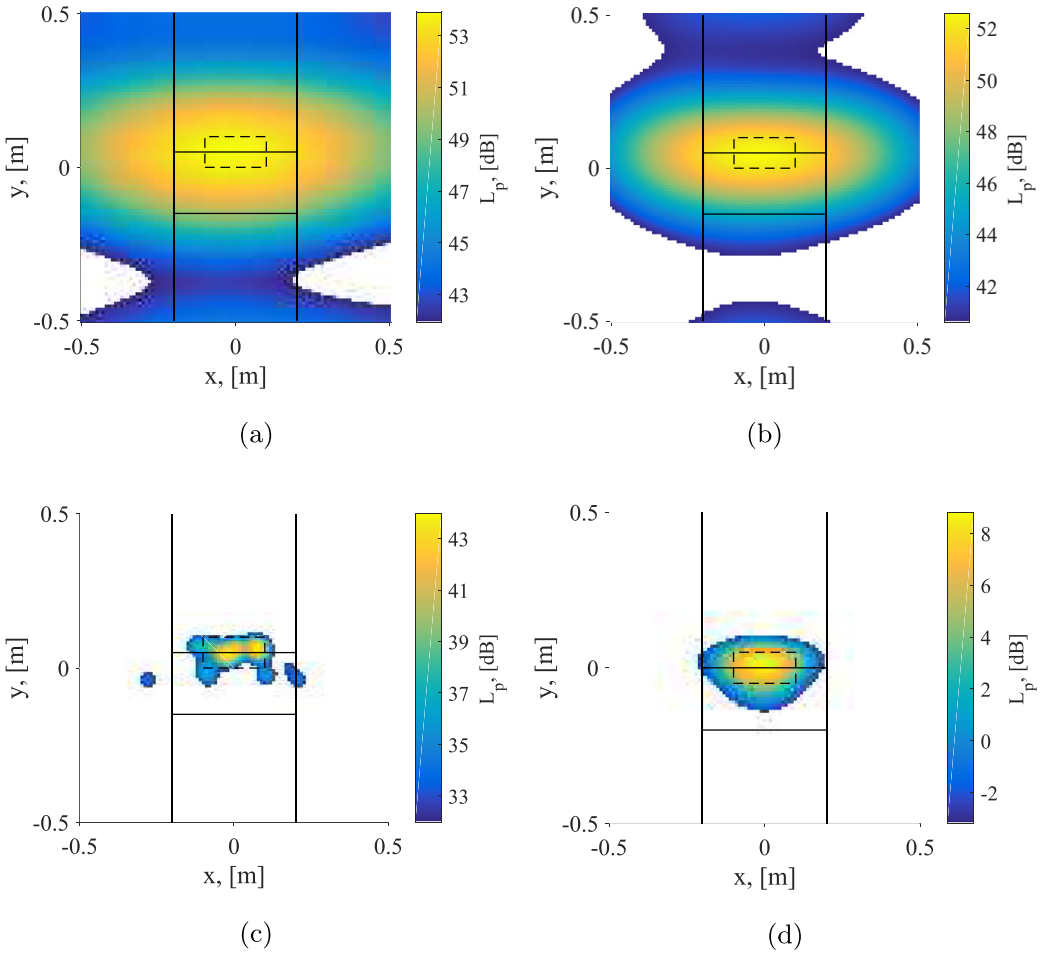

Fig. 13. Source maps for the NACA 0018 airfoil with $V = 40$ m/s for a one–third–octave frequency band centered at 1 kHz for: (a) CFDBF, (b) FUNBF with $\nu = 8$, (c) EHR–CLEAN–SC, and (d) GIBF. The airfoil location and side plates are denoted by a solid rectangle and vertical lines, respectively. The dashed rectangles denote the ROI.

chord. The nominal size of the carborundum elements used in this paper was 0.84 mm, instead of 0.6 mm as in other previous experiments in the same wind tunnel that did not present dominant leading–edge noise [14–16,57]. Hence, this increase in roughness is probably the generating mechanism for leading–edge noise in this experiment.

- The source map obtained from CFDBF (Fig. 14a) shows the presence of the leading edge noise as a dominant noise source followed by what seems to be another line source at about 50% of the airfoil chord, both of them along the whole span. This second line source is, however, not clearly distinguishable due to the insufficient spatial resolution of this method. The trailing edge noise is also present as a secondary line source, as well as other extraneous noise sources (about 4 dB lower than the peak level) on the borders of the source map that could be due to the background noise or sidelobes. In general, for both the leading–edge and trailing–edge noise sources, the peak values are located in the junction with the vertical side plates (i.e., at $x = \pm 0.2$ m). The reason for this is likely the interaction of the boundary layer of the vertical side plates with the corners of the airfoil [62]. The influence of these corner sources is minimized by integrating the results within the selected ROI.
- FUNBF (Fig. 14b) slightly improves the sidelobe level with respect to CFDBF but it shows a very similar source distribution. The sidelobe level could be further improved by removing the main diagonal of the CSM [25] but it was observed that this approach can lead to misleading results at high frequencies. For example, if the leading–edge noise source is stronger than the trailing–edge noise, the presence of the former can reduce the observed values of the latter, especially when using methods that rely on the eigenvalue decomposition of the CSM, such as FUNBF. An extended explanation of this phenomenon can be found in Ref. [23].
- Once again, EHR–CLEAN–SC (Fig. 14c) displays a discontinuous distribution of sound sources, with the presence of two dominant point sources located at the corners of the airfoil at the leading edge and one in the center of the leading edge. A number of secondary sound sources are also detected at about 40% of the chord and along the whole span. The trailing–edge noise source, however, is not detected in this case.

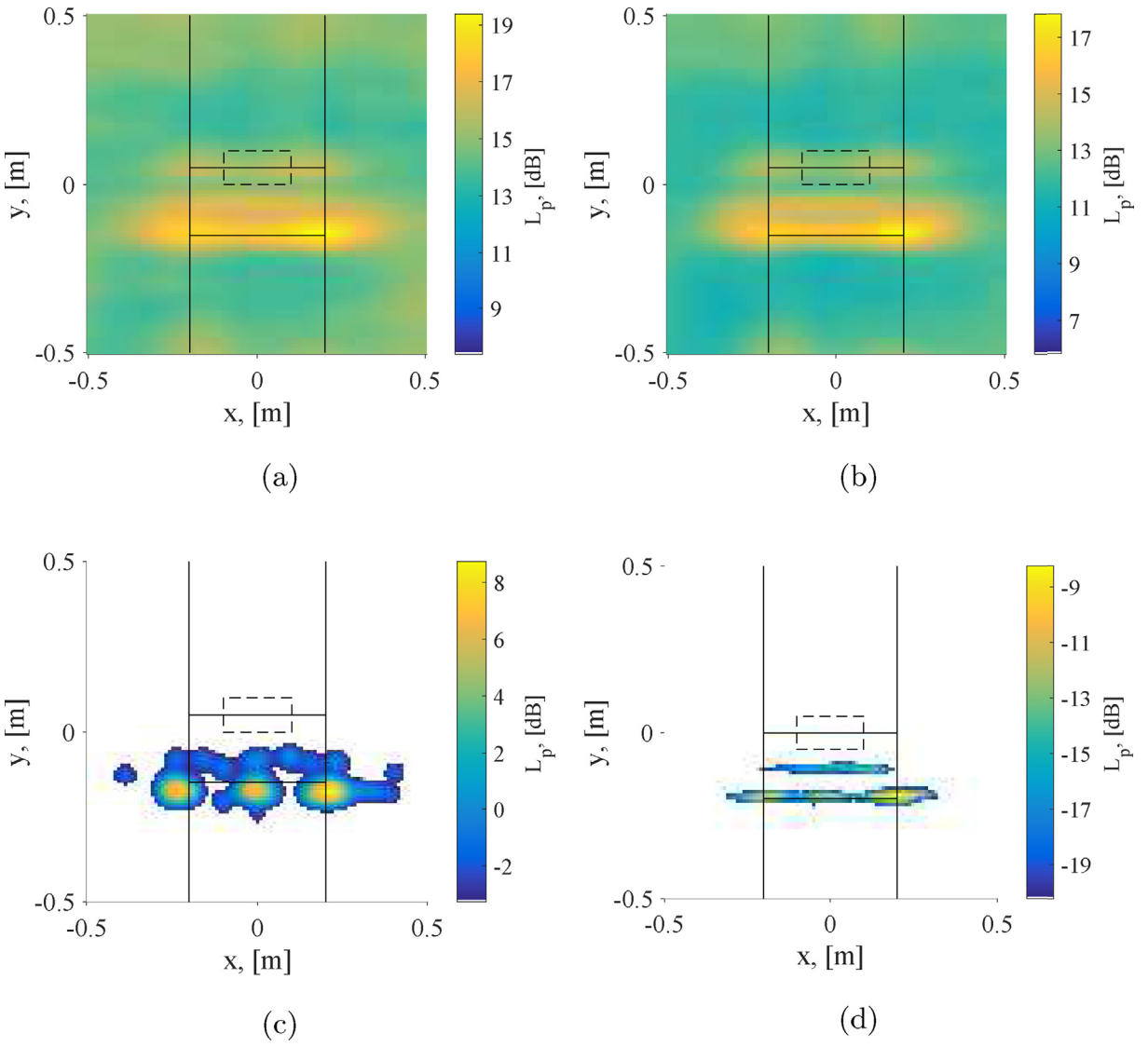

Fig. 14. Source maps for the NACA 0018 airfoil with $V = 20$ m/s for a one–third–octave frequency band centered at 4 kHz for: (a) CFDBF, (b) FUNBF with $\nu = 8$, (c) EHR–CLEAN–SC, and (d) GIBF. The airfoil location and side plates are denoted by a solid rectangle and vertical lines, respectively. The dashed rectangles denote the ROI.

- Finally, GIBF (Fig. 14d) clearly shows the leading–edge as the dominant noise source. A secondary line source is found at about the same position as the secondary point sources in the case of EHR–CLEAN–SC (approximately at 50% of the chord), which could be due to some flow instabilities at that location. The trailing edge noise, on the other hand, is not visible for the selected dynamic range of the color scale, and starts to be visible only if the range is extended to 20 dB.

For the four methods, the leading–edge noise source is not completely symmetric and presents slightly higher values on its right end ($x = 0.2$ m). This is, perhaps, due to the random distribution of the carborundum elements in the tripping tape [59], as mentioned in section 2.

3.3.3. *Frequency spectra*

The source maps obtained by each of the four acoustic imaging methods were integrated within the defined ROI to isolate the trailing–edge noise frequency spectra, as explained in section 1. For CFDBF, the source power integration method extended for line sources (SPIL) [32,33] was employed, since it considers the presence of line sources. The same approach was taken for FUNBF but adapting the formula to the FUNBF expression [8,9]. For the four methods, the integrated results in the ROI considered

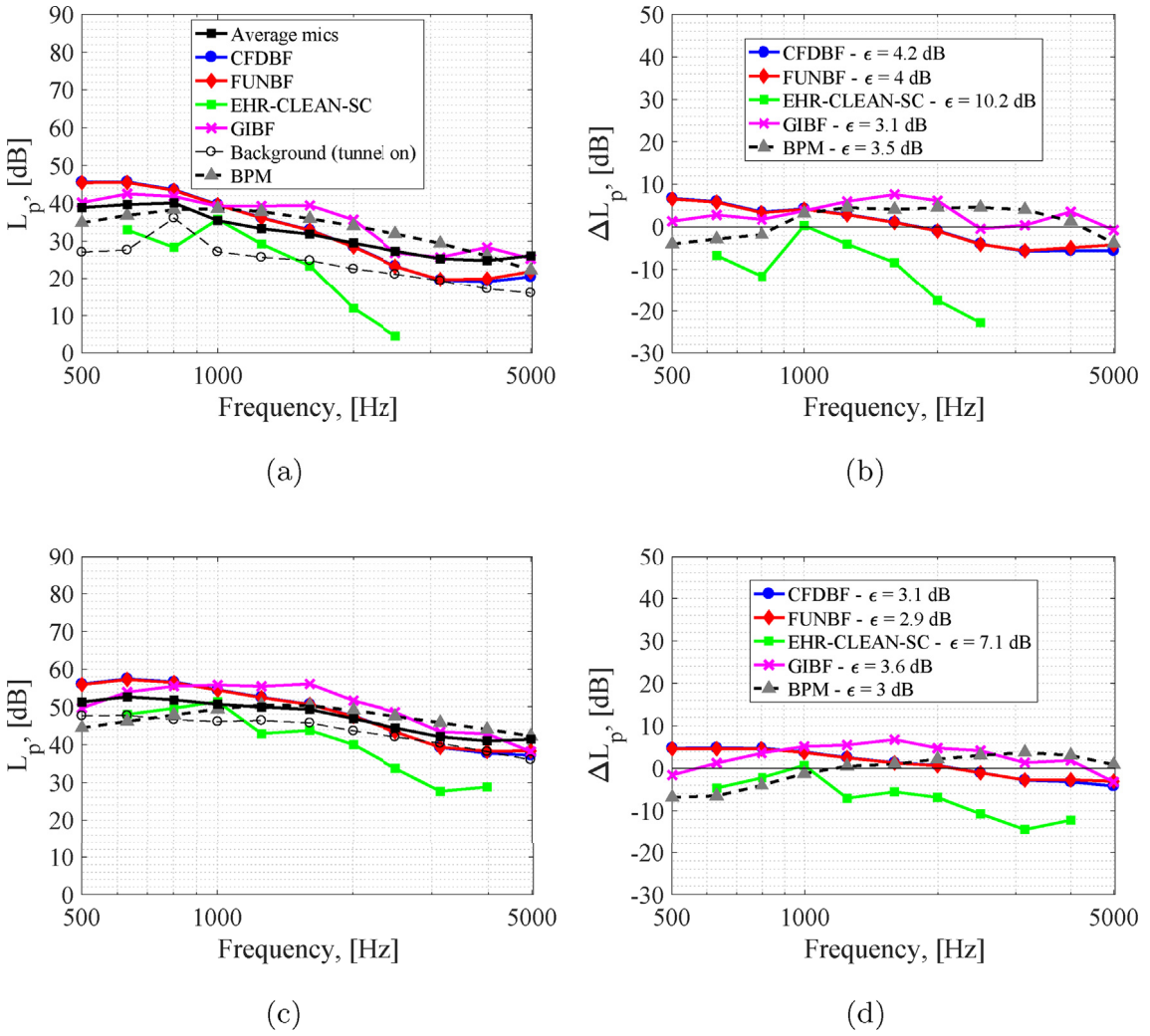

Fig. 15. Left column: One–third–octave band frequency spectra for the NACA 0018 airfoil for all the considered acoustic imaging methods, as well as for the signal recorded by the array (averaged over all microphones), the estimations of the BPM method and the background noise of the facility. Right column: Error per third–octave band made by each acoustic imaging method, with respect to the average microphone signal. The rows refer to different flow velocities: (a) and (b) $V = 20$ m/s, (c) and (d) $V = 40$ m/s.

(with a spanwise length of 0.2 m) were scaled to account for the full span of the airfoil (0.4 m) by adding 3 dB (double power), since the airfoil span is twice the one of the ROI.

The obtained frequency spectra are presented in Fig. 15, as well as for the signal recorded by the array (averaged over all microphones), the estimations of the BPM method [49] and the background noise of the facility (at the corresponding velocities and without the airfoil present). The BPM model is a semi–empirical model based on extensive far–field microphone measurements of a NACA 0012 airfoil for predicting various components of airfoil self–noise, including the turbulent boundary trailing edge noise. The results can be extended to different airfoil geometries, such as for the NACA 0018 case analyzed here. The higher thickness of the NACA 0018 airfoil with respect to the NACA 0012 one is expected to cause slightly higher noise emissions [63]. This model provides the predicted noise spectra in one–third–octave bands based on the given Reynolds number, effective angle of attack, airfoil's chord and span, and the observer's location. The displacement thickness of the boundary layer δ^* is an optional input. In this case, the values for δ^* were estimated using the software XFOIL [64] and were found to be 2.3 mm for $V = 20$ m/s and 2.1 mm for $V = 40$ m/s. The spectra for both flow velocities considered are included: 20 m/s (Figs. 15a) and 40 m/s (Fig. 15c). All the spectra correspond to an observer distance of 1 m from the trailing edge.

On the right in Fig. 15, the differences in sound pressure level ΔL_p with respect to the reference spectrum measured by the array (averaged over all microphones) are depicted. It should be noted that the average signal measured by the array is not just due to the trailing–edge noise but also from other extraneous sources, such as the leading–edge noise (see Fig. 14). However, for the given setup, trailing–edge noise is expected to be the dominant noise source for most of the frequency range [49].

In general, all the acoustic imaging methods employed show a similar trend as the average microphone signal, except for EHR–CLEAN–SC, which provides considerably lower values and even no results for some frequency bands, for which no sources were resolved within the selected ROI because they fell outside of it. This behavior can be explained because this method specifically considers the presence of point sources, instead of distributed sources as trailing–edge noise. The other three methods (CFDBF, FUNBF and GIBF) present similar ϵ values (around 3 dB) as the BPM method for both flow velocities. In general, the overall agreement for the higher flow speed (40 m/s) is closer than for the lower one (20 m/s). If we consider the aforementioned contribution of the leading–edge noise at higher frequencies for the average microphone signal, the solutions provided by CFDBF and FUNBF would present an even closer match to the expected trailing–edge noise spectrum, since they now show negative values of ΔL_{p}. For GIBF, the general overestimation of the spectra could be related to the regularization process for solving the inverse problem. The same regularization approach as for the speakers' case was employed for the airfoil case, which increases the intensity of spurious sources of the map. A proper choice of the regularization parameters in the GIBF algorithm has been indeed proven to be crucial for a correct estimation of the source intensity [45,46].

Since neither the signal of the average microphone signal nor the estimations of the BPM model can be considered as a perfect reference to compare the results with because they also include the contribution of the leading–edge noise, it was decided to assess the expected collapse of the spectra corresponding to both flow velocities once they have their frequency axis normalized using the Strouhal number based on δ^*, $St = f\delta^*/V$ and the sound pressure levels normalized by the following expression [49,65,66]:

$$L_{\mathrm{p,norm}} = L_{\mathrm{p}} - 10\,n\log_{10}\frac{V}{V_{\mathrm{ref}}} - 10\log_{10}\frac{\delta^*}{\delta^*_{\mathrm{ref}}} \tag{1}$$

where V_{ref} is a reference velocity, and δ^*_{ref} and $L_{p,V_{\mathrm{ref}}}$ are the displacement thickness of the boundary layer and the sound pressure level at that same velocity, respectively. The parameter n is the expected dependency of the trailing–edge noise levels with respect to the flow velocity V (see section 3.3.4 below). For this assessment, a value of $n = 4.5$ was used, following the suggestions from literature [49,65,66].

The scaled spectra (both in frequency and L_{p} for the four acoustic imaging methods, the average microphone recordings and the BPM model's estimations are included in Fig. 16. The best collapse of the two normalized spectra is found for the case of the average microphone signal (Fig. 16a), where an average deviation ϵ within the frequency range considered of 0.8 dB is observed. The results provided by the BPM model (Fig. 16b) present a good collapse for $St \geq 0.1$, but a considerable deviation for lower Strouhal numbers causing a value of $\epsilon = 1.9$ dB. From the four acoustic imaging methods used, CFDBF and FUNBF (Fig. 16c and d, respectively) present the closest match between both scaled spectra with $\epsilon \approx 1.5$ dB. EHR–CLEAN–SC (Fig. 16e) shows unexpectedly sharp peaks close to $St \approx 0.11$ and a deviation of $\epsilon \approx 5.2$ dB. Lastly, GIBF exhibits a similar trend as CFDBF and FUNBF but with a considerably larger deviation between both spectra of $\epsilon \approx 3.6$ dB, probably due to the non–optimal regularization process that has been previously discussed.

3.3.4. Dependency of the noise levels with the flow speed

Lastly, the influence of the flow velocity in the emitted far–field noise levels is analyzed. For this purpose, the overall sound pressure level $L_{\mathrm{p,overall}}$ values in the frequency range considered (500 Hz–5 kHz) are employed, i.e., the integrated sound levels in the frequency spectra in Fig. 15.

Figure 17 depicts the $L_{\mathrm{p,overall}}$ values for the four acoustic imaging methods considered, as well as for the average microphone and the BPM method, for both flow velocities. The first thing that can be observed is that there is a positive offset of about 3 dB between the $L_{\mathrm{p,overall}}$ values obtained by CFDBF, FUNBF and GIBF and those measured by the array (averaged over all microphones). The cause of this offset remains unknown, but it could be an artifact of the integration procedure of the source maps by these three methods, or due to the scaling of the integrated results to account for the full airfoil span, as mentioned in section 3.3.3. EHR–CLEAN–SC provides values about 6 dB lower than the reference solution, which can be explained because in the spectra illustrated in Fig. 15 there were some frequency bands for which this method provided no solution. Lastly, the estimations of the BPM model are within less than 1 dB difference with respect to the results of the average microphone, which is expected since the BPM model was developed based on single microphone measurements [49].

Equation (1)) was solved for the parameter n, which was calculated for the four acoustic imaging methods, as well as for the average microphone and the BPM model, see Fig. 17. The n values in this experiment were calculated by only considering the two flow velocities employed (20 m/s and 40 m/s). The experiments of Brooks et al. [49] provided n values between 4.5 and 5, depending on the flow velocity. According to Howe [67] $n = 4.6$, whereas Oerlemans et al. [65,66] found that broadband trailing–edge noise scales with $n = 4.5$.

The results by the average microphone scale with $n = 4.73$, whereas CFDBF and FUNBF both present a value of $n = 4.52$, which is almost the same as the expected value of 4.5. The BPM method offers an relatively low value ($n = 4.27$), whereas GIBF provides $n = 4.95$. Lastly, EHR–CLEAN–SC gives a value of $n = 5.69$, which is higher than expected, but it was calculated with the incomplete spectra provided by this method, see Fig. 15. It should be considered that only a limited frequency range (500 Hz–5 kHz) is being taken into account and that using only two points for calculating a fit is not very accurate. Therefore, considering measurements taken at more velocities for estimating n is recommended for obtaining more reliable results.

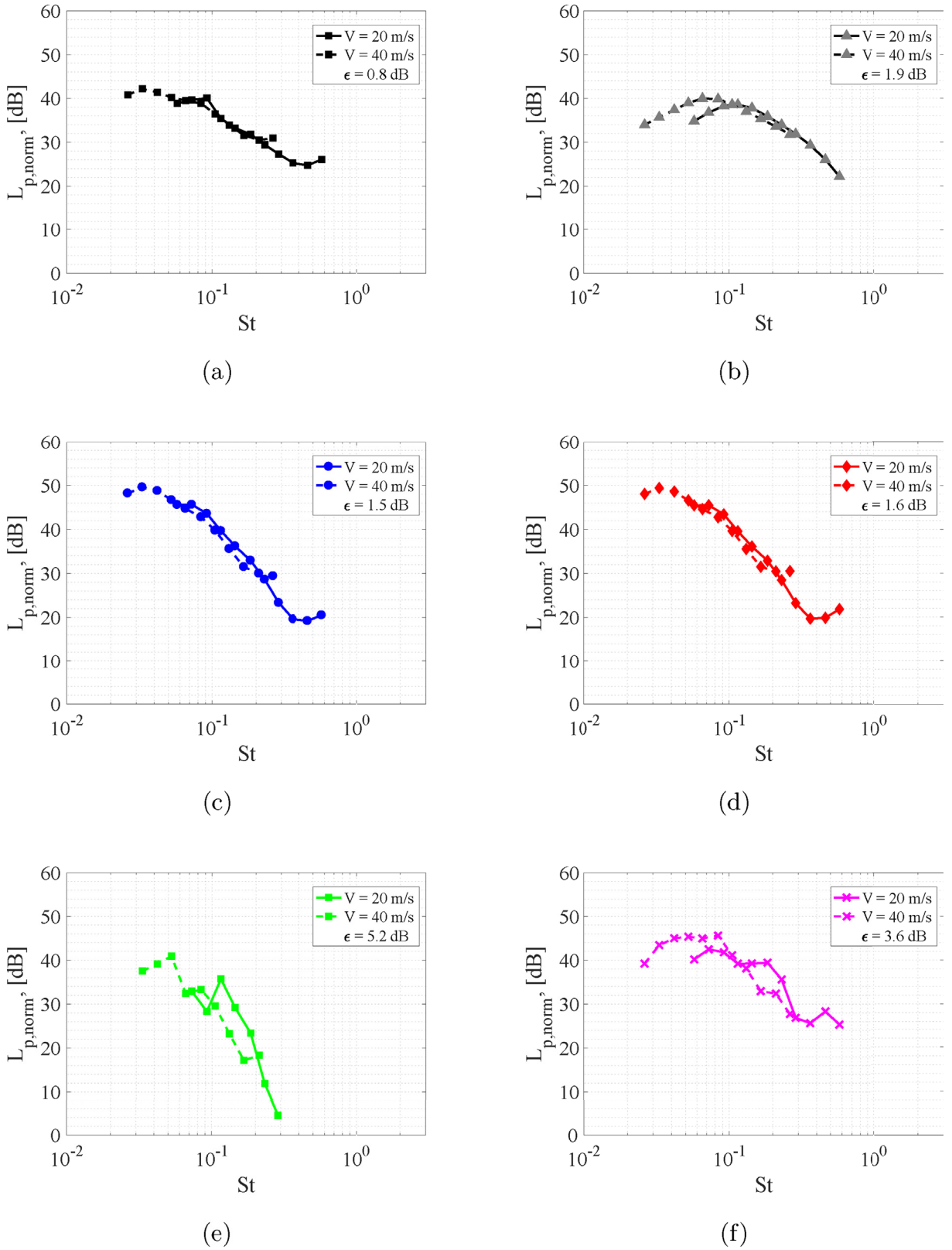

Fig. 16. Collapse of the normalized one–third–octave band frequency spectra for both flow speeds for the NACA 0018 airfoil and: (a) the average microphone signal, (b) the BPM method, (c) CFDBF, (d) FUNBF with $\nu = 8$, (e) EHR–CLEAN–SC, and (f) GIBF.

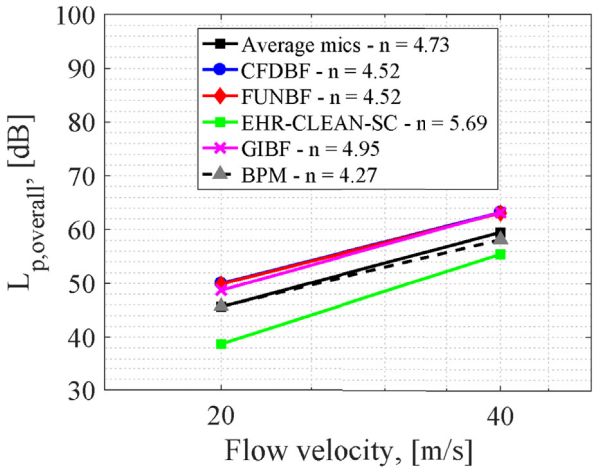

Fig. 17. Dependence between the overall trailing–edge noise levels (between 500 Hz and 5 kHz) and the flow velocity for all the acoustic imaging methods considered for the NACA 0018 airfoil, as well as for the average microphone and the BPM method. Note the logarithmic scale in the velocity axis.

3.4. Summary of the errors for each case

In order to summarize the main results regarding source power estimation of the three test cases in a single figure, Fig. 18a presents a bar plot of the average errors ϵ made by each acoustic imaging method for the experiments featuring: one speaker, two speakers and the NACA 0018 airfoil. It should be reminded that these errors are with respect to the signal measured by the average microphone, and that implies some limitations that have been mentioned throughout the text. The average errors displayed in the bar plot in Fig. 18a have been calculated by averaging linearly the errors of all the *subcases* analyzed, i.e., the four SNR values for the one speaker case, the four different volumes for the two–speaker case, and both flow velocities for the NACA 0018 airfoil case. Moreover, the agreement between the normalized spectra following the Strouhal scaling, see Fig. 16, for the NACA 0018 airfoil experiment and for the six approaches is represented in Fig. 18b.

In general, it can be observed that GIBF and EHR–CLEAN–SC are the best methods for the cases involving point sources (i.e., speakers). GIBF provides slightly lower average errors and EHR–CLEAN–SC shows a better rendering of the source maps for the case with two speakers placed closer than the Rayleigh resolution limit. For the airfoil case CFDBF and FUNBF (with their respective integration techniques) provide the best agreements and render the expected line source distribution. Similar results were obtained in a benchmark exercise of a simulated line source modeling a trailing–edge noise measurement in a closed–section wind tunnel [26,32,33].

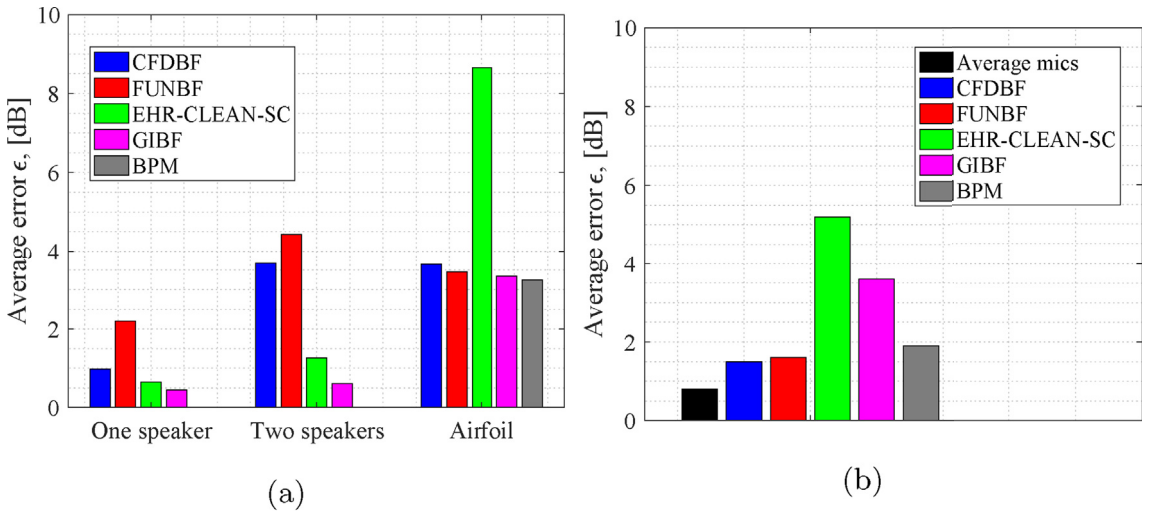

Fig. 18. (a) Average errors ϵ made by each of the acoustic imaging methods considered for the three experimental cases analyzed. (b) Average collapse error for the expected Strouhal scaling for trailing–edge noise.

4. Conclusions

The performance of four acoustic imaging methods was investigated in this paper in terms of accuracy and variability for the purpose of aeroacoustic measurements featuring microphone arrays: the standard conventional frequency domain beamforming (CFDBF), functional beamforming (FUNBF), the enhanced high–resolution version of CLEAN–SC (EHR–CLEAN–SC) and generalized inverse beamforming (GIBF). Three different experimental test cases were measured inside of an anechoic wind tunnel and analyzed using each method: 1) one speaker emitting synthetic broadband noise at low signal to noise ratio with respect to the background noise, 2) two closely–located speakers emitting incoherent synthetic broadband noise signals at different relative volumes and 3) trailing–edge noise of a tripped NACA 0018 airfoil.

For the case of a single speaker, it was observed that GIBF is the best–performing method, followed closely by EHR–CLEAN–SC. The repeatability of these results was investigated in ten repetitions and it was confirmed that the four acoustic imaging methods present basically the same standard deviation as the signal emitted itself (below 1 dB). Only GIBF and EHR–CLEAN–SC require some extra care from the user when selecting the number of expected sound sources in the experiment, but that parameter can be easily iterated for.

When two incoherent speakers are considered EHR–CLEAN–SC provides the source maps with the best quality at low frequencies, below the Rayleigh resolution limit. In terms of average errors, GIBF has again the lowest errors with respect to the reference signal followed closely by EHR–CLEAN–SC, whereas CFDBF and FUNBF have some troubles for retrieving the correct emitted sound levels, due to their insufficient spatial resolution.

Lastly, for the case of trailing–edge noise, CFDBF and FUNBF render the most physically relevant source distributions. GIBF provides better dynamic range but more erratic distributions, whereas EHR–CLEAN–SC presents clusters of point noise sources instead of the expected line source along the trailing edge, which sometimes fall outside of the ROI, providing no solutions at some frequencies. Moreover, CFDBF and FUNBF show the closest agreement between the scaled spectra, followed by GIBF. The dependencies of the noise levels with the flow speed measured by CFDBF, FUNBF and GIBF agree with the expected trends from literature. EHR–CLEAN–SC does not seem to be suitable for this application case.

In this research, it was shown that more complex deconvolution and inverse methods such as EHR–CLEAN–SC and GIBF, respectively, are the best choices when closely–spaced point sources are present, such as for landing gear noise. In case distributed sound sources are expected, such as leading– or trailing–edge noise, CFDBF and FUNBF (with their respective integration techniques) are the most suitable methods.

References

[1] R. Merino-Martinez, Microphone Arrays for Imaging of Aerospace Noise Sources, Ph.D. thesis Delft University of Technology, 2018. ISBN: 978-94-028-1301-2, https://repository.tudelft.nl/islandora/object/uuid:a3231ea9-1380-44f4-9a93-dbbd9a26f1d6?collection=research.

[2] M. Snellen, R. Merino-Martinez, D.G. Simons, Assessment of aircraft noise sources variability using an acoustic camera, in: 5th CEAS Air & Space Conference. Challenges in European Aerospace. September 7-11, 2015, Council of European Aerospace Societies, Delft, Netherlands, 2015 2015-019, http://repository.tudelft.nl/assets/uuid:d63eab6c-4cab-4ab2-ac14-d13d91837443/319502.pdf.

[3] M. Snellen, R. Merino-Martinez, D.G. Simons, Assessment of noise level variability on landing aircraft using a phased microphone array, J. Aircr. 54 (6) (2017) 2173–2183, http://dx.doi.org/10.2514/1.C033950.

[4] R. Merino-Martinez, M. Snellen, D.G. Simons, Functional beamforming applied to imaging of flyover noise on landing aircraft, J. Aircr. 53 (6) (2016) 1830–1843, http://arc.aiaa.org/doi/abs/10.2514/1.C033691.

[5] R. Merino-Martinez, M. Snellen, D.G. Simons, Functional beamforming applied to full scale landing aircraft, in: 6th Berlin Beamforming Conference, February 29 - March 1 2016, Berlin, Germany, GFaI, e.V., Berlin, 2016, BeBeC-2016-D12., http://www.bebec.eu/Downloads/BeBeC2016/Papers/BeBeC-2016-D12.pdf.

[6] R. Merino-Martinez, L. Bertsch, M. Snellen, D.G. Simons, Analysis of landing gear noise during approach, in: 22nd AIAA/CEAS Aeroacoustics Conference. May 30 - June 1 2016, Lyon, France, AIAA, 2016. AIAA paper 2016-2769, http://arc.aiaa.org/doi/pdf/10.2514/6.2016-2769.

[7] R. Merino-Martinez, M. Snellen, D.G. Simons, Determination of aircraft noise variability using an acoustic camera, in: 23rd International Congress on Sound and Vibration, July 10 - 14 2016, Athens, Greece, International Inst. of Acoustics and Vibration (IIAV), Auburn, Alabama, USA, 2016, http://iiav.org/archives_icsv_last/2016_icsv23/content/papers/papers/full_paper_164_20160518160041692.pdf.

[8] R. Merino-Martinez, E. Neri, M. Snellen, J. Kennedy, D.G. Simons, G.J. Bennett, Comparing flyover noise measurements to full-scale nose landing gear wind-tunnel experiments for regional aircraft, in: 23rd AIAA/CEAS Aeroacoustics Conference. June 5 - 9 2017. Denver, Colorado, USA, AIAA, 2017. AIAA paper 2017-3006, http://arc.aiaa.org/doi/pdf/10.2514/6.2017-3006.

[9] R. Merino-Martinez, E. Neri, M. Snellen, J. Kennedy, D.G. Simons, G.J. Bennett, Analysis of nose landing gear noise comparing numerical computations, prediction models and flyover and wind-tunnel measurements, in: 24th AIAA/CEAS Aeroacoustics Conference. June 25 - 29 2018. Atlanta, Georgia, USA, AIAA, 2018. AIAA paper 2018-3299, http://arc.aiaa.org/doi/pdf/10.2514/6.2018-3299.

[10] R. Merino-Martinez, A. Vieira, M. Snellen, D.G. Simons, Sound quality metrics applied to aircraft components under operational conditions using a microphone array, in: 25th AIAA/CEAS Aeroacoustics Conference. May 20 - 24 2019. Delft, The Netherlands, AIAA, 2019. AIAA paper 2019-2513, http://arc.aiaa.org/doi/pdf/10.2514/6.2019-2513.

[11] R. Merino-Martinez, S.J. Heblij, D.H.T. Bergmans, M. Snellen, D.G. Simons, Improving aircraft noise predictions by considering the fan rotational speed, J. Aircr. 56 (1) (2019) 284–294, http://arc.aiaa.org/doi/abs/10.2514/1.C034849.

[12] R. Merino-Martinez, M. Snellen, D.G. Simons, Calculation of the fan rotational speed based on flyover recordings for improving aircraft noise prediction models, in: 23rd International Congress on Acoustics. September 9 - 13 2019. Aachen, Germany, ICA, 2019, http://pub.dega-akustik.de/ICA2019/data/articles/000463.pdf.

[13] S. Oerlemans, Detection of Aeroacoustic Sound Sources on Aircraft and Wind Turbines, Ph.D. thesis University of Twente, Enschede, the Netherlands, 2009, http://doc.utwente.nl/67363/1/thesis_S_Oerlemans.pdf.

[14] C. Arce Leon, R. Merino-Martinez, D. Ragni, F. Avallone, M. Snellen, Boundary layer characterization and acoustic measurements of flow-aligned trailing edge serrations, Exp. Fluid 57 (182) (2016) 1–22, http://link.springer.com/10.1007/s00348-016-2272-z.

[15] C. Arce Leon, R. Merino-Martinez, D. Ragni, F. Avallone, F. Scarano, S. Prbsting, M. Snellen, D.G. Simons, J. Madsen, Effect of trailing edge serration-flow misalignment on airfoil noise emission, J. Sound Vib. 405 (2017) 19–33, http://dx.doi.org/10.1016/j.jsv.2017.05.035.

[16] C. Arce Leon, R. Merino-Martinez, S. Probsting, D. Ragni, F. Avallone, Acoustic emissions of semipermeable trailing edge serrations, Acoust Aust. 46 (1) (2017) 111–117, https://link.springer.com/article/10.1007%2Fs40857-017-0093-8.

[17] A. Rubio Carpio, R. Merino-Martinez, F. Avallone, D. Ragni, M. Snellen, S. van der Zwaag, Broadband trailing edge noise reduction using permeable metal foams, in: 46th International Congress and Exposition of Noise Control Engineering, 27 - 30 August, 2017, Hong Kong, InterNoise, 2017, https://repository.tudelft.nl/islandora/object/uuid%3Aedae7923-d41c-4169-ae9d-65a8e02eb583?collection=research.

[18] A. Rubio Carpio, R. Merino-Martinez, F. Avallone, D. Ragni, M. Snellen, S. van der Zwaag, Experimental characterization of the turbulent boundary layer over a porous trailing edge for noise abatement, J. Sound Vib. 443 (2019) 537–558, https://doi.org/10.1016/j.jsv.2018.12.010.

[19] R. Merino-Martinez, R. Pieren, M. Snellen, D.G. Simons, Assessment of the sound quality of wind turbine noise reduction measures, in: 26th International Congress on Sound and Vibration, July 7 - 11 2019, Montreal, Canada, International Inst. of Acoustics and Vibration (IIAV), Auburn, Alabama, USA., 2019.

[20] L.C. Caldas, P.C. Greco, C.C.J. Pagani, L.A. Baccala, Comparison of different techniques for rotating beamforming at the university of Sao Paulo fan rig test facility, in: 6th Berlin Beamforming Conference, February 29 - March 1 2016, Berlin, Germany, GFaI, e.V., Berlin, 2016 BeBeC-2016-D14, http://www.bebec.eu/Downloads/BeBeC2016/Papers/BeBeC-2016-D14.pdf.

[21] G. Herold, E. Sarradj, Frequency domain deconvolution for rotating sources on an axial fan, in: 6th Berlin Beamforming Conference, February 29 - March 1 2016, Berlin, Germany, GFaI, e.V., Berlin, 2016 BeBeC-2016-D18, http://www.bebec.eu/Downloads/BeBeC2016/Papers/BeBeC-2016-D18.pdf.

[22] T. Sinnige, B. Della Corte, R. de Vries, F. Avallone, R. Merino-Martinez, D. Ragni, G. Eitelberg, L.L.M. Veldhuis, Alleviation of propeller-slipstream-induced unsteady pylon loading by a flow-permeable leading edge, J. Aircr. 56 (3) (2019) 1214–1230, http://arc.aiaa.org/doi/abs/10.2514/1.C035250.

[23] R. Merino-Martinez, P. Sijtsma, M. Snellen, T. Ahlefeldt, J. Antoni, C.J. Bahr, D. Blacodon, D. Ernst, A. Finez, S. Funke, T.F. Geyer, S. Haxter, G. Herold, X. Huang, W.M. Humphreys, Q. Leclere, A. Malgoezar, U. Michel, T. Padois, A. Pereira, C. Picard, E. Sarradj, H. Siller, D.G. Simons, C. Spehr, A review of acoustic imaging methods using phased microphone arrays (part of the Aircraft Noise Generation and Assessment special issue), CEAS Aeronautical Journal 10 (1) (2019) 197–230, https://rdcu.be/brsL2.

[24] T. Mueller, Aeroacoustic Measurements, Springer Science & Business Media, 2002. ISBN: 978-3-642-07514-8, https://books.google.com/books?hlen&lr&id MU6WLXFJLWgC&pgis1.

[25] P. Sijtsma, Phased array beamforming applied to wind tunnel and flyover tests. Tech. Rep. NLR-TP-2010-549, National Aerospace Laboratory (NLR), Anthony Fokkerweg 2, 1059 CM Amsterdam, P.O. Box 90502, 1006 BM Amsterdam, The Netherlands (December 2010), https://reports.nlr.nl/xmlui/bitstream/handle/10921/192/TP-2010-549.pdf?sequence1.

[26] E. Sarradj, G. Herold, P. Sijtsma, R. Merino-Martinez, A.M.N. Malgoezar, M. Snellen, T.F. Geyer, C.J. Bahr, R. Porteous, D.J. Moreau, C.J. Doolan, A microphone array method benchmarking exercise using synthesized input data, in: 23rd AIAA/CEAS Aeroacoustics Conference. June 5 - 9 2017. Denver, CO, USA, AIAA, 2017. AIAA paper 2017-3719, http://arc.aiaa.org/doi/pdf/10.2514/6.2017-3719.

[27] E. Sarradj, Threedimensional acoustic source mapping with different beamforming steering vector formulations, Advances in Acoustics and Vibration 2012 (292695) (2012) 1–12, http://dx.doi.org/10.1155/2012/292695.

[28] E. Sarradj, G. Herold, S. Jekosch, Array methods: which one is the best? in: 7th Berlin Beamforming Conference, March 5 - 6 2018, Berlin, Germany, GFaI, e.V., Berlin, 2018, BeBeC-2018-S01, http://www.bebec.eu/Downloads/BeBeC2018/Papers/BeBeC-2018-S01.pdf.

[29] B.D. van Veen, K.M. Buckley, Beamforming: a versatile approach to spatial filtering, IEEE ASSP Mag. 5 (2) (1988) 4–24, http://ieeexplore.ieee.org/document/665/.

[30] D.H. Johnson, D.E. Dudgeon, Array Signal Processing, Concepts and Techniques, P T R Prentice Hall, Englewood Cliffs, 1993. ISBN: 978-0130485137, https://books.google.nl/books/about/Array_Signal_Processing.html?idv_NSAAAAMAAJ&redir_escy.

[31] F.R.S. Lord Rayleigh, XXXI Investigations in optics with special reference to the spectroscope, the london, edinburgh and dublin, Philosophical Magazine and Journal of Science 8 (49) (1879) 261–274, https://dx.doi.org/10.1080/14786447908639684.

[32] R. Merino-Martinez, P. Sijtsma, M. Snellen, Inverse integration method for distributed sound sources, in: 7th Berlin Beamforming Conference, March 5 - 6 2018, Berlin, Germany, GFaI, e.V., Berlin, 2018, BeBeC-2018-S07, https://www.bebec.eu/Downloads/BeBeC2018/Papers/BeBeC-2018-S07.pdf.

[33] R. Merino-Martinez, P. Sijtsma, A. Rubio Carpio, R. Zamponi, S. Luesutthiviboon, A.M.N. Malgoezar, M. Snellen, C. Schram, D.G. Simons, Integration methods for distributed sound sources, Int. J. Aeroacoustics 18 (45) (2019) 444–469, https://doi.org/10.1177/1475472X19852945.

[34] T.F. Brooks, W.M. Humphreys, Effect of directional array size on the measurement of airframe noise components, in: 5th AIAA/CEAS Aeroacoustics Conference, Bellevue, WA, USA, 1999. AIAA paper 1999-1958, http://arc.aiaa.org/doi/pdf/10.2514/6.1999-1958.

[35] R.P. Dougherty, Functional beamforming, in: 5th Berlin Beamforming Conference, February 19 - 20 2014, Berlin, Germany, GFaI, e.V., Berlin, 2014, BeBeC-2014-01, http://bebec.eu/Downloads/BeBeC2014/Papers/BeBeC-2014-01.pdf.

[36] R.P. Dougherty, Functional beamforming for aeroacoustic source distributions, in: 20th AIAA/CEAS Aeroacoustics Conference. June 16 20 2014. Atlanta GA, USA, 2014https://doi.org/10.2514/6.2014-3066. AIAA paper 2014-3066.

[37] P. Sijtsma, M. Snellen, High-Resolution CLEAN-SC, in: 6th Berlin Beamforming Conference, February 29 - March 1 2016, Berlin, Germany, GFaI, e.V., Berlin, 2016, BeBeC-2016-S1, http://www.bebec.eu/Downloads/BeBeC2016/Papers/BeBeC-2016-S1.pdf.

[38] P. Sijtsma, R. Merino-Martinez, A.M.N. Malgoezar, M. Snellen, High-Resolution CLEAN-SC: theory and experimental validation, Int. J. Aeroacoustics 16 (45) (2017) 274–298. SAGE Publications Ltd. London, United Kingdom, http://journals.sagepub.com/doi/10.1177/1475472X17713034.

[39] P. Sijtsma, R. Merino-Martinez, A.M.N. Malgoezar, M. Snellen, High-Resolution CLEAN-SC: theory and experimental validation, in: 23rd AIAA/CEAS Aeroacoustics Conference. June 5 - 9 2017. Denver, Colorado, USA, AIAA, 2017. AIAA paper 2017-3841, http://arc.aiaa.org/doi/pdf/10.2514/6.2017-3841.

[40] S. Luesutthiviboon, A. Malgoezar, M. Snellen, P. Sijtsma, D.G. Simons, Improving source discrimination performance by using an optimized acoustic array and Adaptive-High-Resolution CLEAN-SC beamforming, in: 7th Berlin Beamforming Conference, March 5 - 6 2018, Berlin, Germany, GFaI, e.V., Berlin, 2018, BeBeC-2018-D07, http://www.bebec.eu/Downloads/BeBeC2018/Papers/BeBeC-2018-D07.pdf.

[41] S. Luesutthiviboon, A.M.N. Malgoezar, R. Merino-Martinez, M. Snellen, P. Sijtsma, D.G. Simons, Enhanced HR-CLEAN-SC for resolving multiple closely spaced sound sources, Int. J. Aeroacoustics 18 (45) (2019) 392–413, https://doi.org/10.1177/1475472X19852938.

[42] P. Sijtsma, CLEAN based on spatial source coherence, Int. J. Aeroacoustics 6 (4) (2007) 357–374. SAGE Publications Ltd. London, United Kingdom, http://dx.doi.org/10.1260/147547207783359459.

[43] T. Suzuki, L_1 generalized inverse beamforming algorithm resolving coherent/incoherent, distributed and multipole sources, J. Sound Vib. 330 (24) (2011) 5835–5851, https://doi.org/10.1016/j.jsv.2011.05.021, http://www.sciencedirect.com/science/article/pii/S0022460X11004068.

[44] T. Suzuki, B. Day, Comparative study on modeidentification algorithms using a phased-array system in a rectangular duct, J. Sound Vib. 347 (2015) 27–45, http://dx.doi.org/10.1016/j.jsv.2013.06.027.

[45] R. Zamponi, N. van de Wyer, C. Schram, An improved regularization of the generalized inverse beamforming applied to a benchmark database, in: 7th Berlin Beamforming Conference, March 5 - 6 2018, Berlin, Germany, GFaI, e.V., Berlin, 2018, BeBeC-2018-D09, http://www.bebec.eu/Downloads/BeBeC2018/Papers/BeBeC-2018-D09.pdf.

[46] R. Zamponi, N. van de Wyer, C. Schram, Benchmark assessment of an improved regularization technique for generalized inverse beamforming, in: 24th AIAA/CEAS Aeroacoustics Conference. June 25 - 29 2018. Atlanta, Georgia, USA, AIAA, 2018. AIAA paper 2018-4106, http://arc.aiaa.org/doi/pdf/10.2514/6.2018-4106.

[47] S. Jekosch, E. Sarradj, G. Herold, T.F. Geyer, Comparison of different solvers for general inverse beamforming algorithms for high resolution aeroacoustic source characterization, in: 7th Berlin Beamforming Conference, March 5 - 6 2018, Berlin, Germany, GFaI, e.V., Berlin, 2018, BeBeC-2018-D08, http://www.bebec.eu/Downloads/BeBeC2018/Papers/BeBeC-2018-D08.pdf.

[48] C.J. Bahr, W.M. Humphreys, D. Ernst, T. Ahlefeldt, C. Spehr, A. Pereira, Q. Leclere, C. Picard, R. Porteus, D.J. Moreau, J. Fischer, C.J. Doolan, A comparison of microphone phased array methods applied to the study of airframe noise in wind tunnel testing, in: 23rd AIAA/CEAS Aeroacoustics Conference. June 5 - 9 2017. Denver, CO, USA, AIAA, 2017. AIAA paper 2017-3718, http://arc.aiaa.org/doi/pdf/10.2514/6.2017-3718.

[49] T.F. Brooks, D.S. Pope, M.A. Marcolini, Airfoil Self-Noise and Prediction, NASA Reference Publication 1218, 1989. Tech. Rep. NASA Reference Publication 1218, https://ntrs.nasa.gov/archive/nasa/casi.ntrs.nasa.gov/19890016302.pdf.
[50] R.P. Dougherty, Cross spectral matrix diagonal optimization, in: 6th Berlin Beamforming Conference, February 29 - March 1, 2016, Berlin, Germany, GFaI, e.V., Berlin, 2016, BeBeC-2016-S2, http://www.bebec.eu/Downloads/BeBeC2016/Papers/BeBeC-2016-S2.pdf.
[51] R. Merino-Martinez, A. Rubio Carpio, C. H. C. Vlemmix, F. Avallone, M. Kotsonis, D. Ragni, Aeroacoustic design and characterization of a vertical open-jet anechoic wind tunnel, AIAA Journal (Manuscript in preparation).
[52] Flamex basic acoustic absorbing foam. accessed in March 2017, https://www.merford.com/media/202626/flamex-basic.pdf.
[53] G.R.A.S., Sound & Vibration 40PH CCP Freefield array microphone. accessed in March 2017, http://www.gras.dk/products/special-microphone/array-microphones/product/178-40ph.
[54] G.R.A.S., Sound & vibration 42AA pistonphone class 1. accessed in March 2017, https://www.gras.dk/products/calibration-equipment/reference-calibrator/product/255-42aa.
[55] Visaton speaker K 50 SQ 8 Ohm,. http://www.visaton.de/en/products/fullrange-systems/k-50-sq-8-ohm accessed in March 2017.
[56] P.D. Welch, The use of fast fourier transform for the estimation of power spectra: a method based on time averaging over short, modified periodograms, IEEE Trans. Audio Electroacoust. (2) (1967) 70–73, https://doi.org/10.1109/TAU.1967.1161901. AU15, http://ieeexplore.ieee.org/stamp/stamp.jsp?arnumber=1161901.
[57] C. Arce Leon, R. Merino-Martinez, D. Ragni, S. Prbsting, F. Avallone, A. Singh, J. Madsen, Trailing edge serrations - Effect of their flap angle on flow and acoustics, in: 7th International Meeting on Wind Turbine Noise, May 2 - 5 2017, Rotterdam, the Netherlands, INCE Europe, 2017, http://pure.tudelft.nl/ws/files/34525999/Trailing_Edge_Serrations_Effect_of_Their_Flap_Angle.pdf.
[58] J.D.J. Anderson, Fundamentals of Aerodynamics, third ed., McGraw-Hill Series in Aeronautical and Aerospace Engineering, 2001. ISBN: 0-07-237335-0, https://avionicsengineering.files.wordpress.com/2016/11/john-d-anderson-jr-fundamentals-of-aerodynamics.pdf.
[59] A.L. Braslow, R.M. Hicks, R.V. Harris Jr., Use of Grit-type Boundary-Layer Transition Trips on Wind-Tunnel Models, NASA, September 1966. Tech. Rep. NASATND3579, NASA Technical Note (D3579), https://ntrs.nasa.gov/archive/nasa/casi.ntrs.nasa.gov/19660026829.pdf.
[60] J. R. Underbrink, Circularly symmetric, zero redundancy, planar array having broad frequency range applications (U.S. Patent number 6,205,224 B1. 2001). URL https://docs.google.com/viewer?urlpatentimages.storage.googleapis.com/pdfs/US6205224.pdf.
[61] R.P. Dougherty, Mutual incoherence of broadband duct acoustic modes, in: 22nd AIAA/CEAS Aeroacoustics Conference. May 30 - June 1 2015. Lyon, France, AIAA, 2016. AIAA paper 2016-3032, http://arc.aiaa.org/doi/pdf/10.2514/6.2016-3032.
[62] M. Tuinstra, P. Sijtsma, Suppression of spurious noise sources in airfoil self-noise measurements, in: 21st AIAA/CEAS Aeroacoustics Conference. June 22 - 26 2015. Dallas, TX, USA, AIAA, 2015. AIAA paper 2015-2689, http://arc.aiaa.org/doi/pdf/10.2514/6.2015-2689.
[63] R. Merino-Martinez, M.P.J. Sanders, L.C. Caldas, F. Avallone, D. Ragni, L.D. de Santana, M. Snellen, D.G. Simons, Comparison between analog and digital microphone phased arrays for aeroacoustic measurements, in: 24th AIAA/CEAS Aeroacoustics Conference. June 25 - 29 2018. Atlanta, Georgia, USA, AIAA, 2018. AIAA paper 2018-2809, http://arc.aiaa.org/doi/pdf/10.2514/6.2018-2809.
[64] M. Drela, part of Lecture Notes in Engineering book series. XFOIL: An Analysis and Design System for Low Reynolds Number Airfoils, 54, Springer Berlin Heidelberg, 1989, pp. 1–12. ISBN: 978-3-642-84010-4., https://link.springer.com/chapter/10.10072F978-3-642-84010-4_1.
[65] S. Oerlemans, Wind Tunnel Aeroacoustic Tests of Six Airfoils for Use on Small Wind Turbines, Tech. Rep. NREL/SR-500-35339. National Renewable Energy Laboratory, August 2004. 1617 Cole Boulevard, Golden, Colorado. 804013393. United States of America, https://www.nrel.gov/docs/fy04osti/35339.pdf.
[66] S. Oerlemans, P. Migliore, Aeroacoustic wind tunnel tests of wind turbine airfoils, in: 10th AIAA/CEAS Aeroacoustics Conference, May 10 - 12, 2004, Manchester, United Kingdom, AIAA, 2004. AIAA paper 2004-3042, https://arc.aiaa.org/doi/pdf/10.2514/6.2004-3042.
[67] M.S. Howe, A review of the theory of trailing edge noise, J. Sound Vib. 61 (3) (1978) 437–465, https://doi.org/10.1016/0022-460X(78)90391-7.